

Tensor N -tubal rank and its convex relaxation for low-rank tensor recovery

Yu-Bang Zheng^a, Ting-Zhu Huang^{a,*}, Xi-Le Zhao^a, Tai-Xiang Jiang^a, Teng-Yu Ji^b, Tian-Hui Ma^c

^a*School of Mathematical Sciences/Research Center for Image and Vision Computing, University of Electronic Science and Technology of China, Chengdu, Sichuan 611731, P.R.China*

^b*School of Science, Northwestern Polytechnical University, Xi'an, Shaanxi 710072, P.R.China.*

^c*School of Mathematics and Statistics, Xi'an Jiaotong University, Xi'an, Shaanxi 710049, P.R.China.*

Abstract

As low-rank modeling has achieved great success in tensor recovery, many research efforts devote to defining the tensor rank. Among them, the recent popular tensor tubal rank, defined based on the tensor singular value decomposition (t-SVD), obtains promising results. However, the framework of the t-SVD and the tensor tubal rank are applicable only to three-way tensors and lack of flexibility to handle different correlations along different modes. To tackle these two issues, we define a new tensor unfolding operator, named mode- k_1k_2 tensor unfolding, as the process of lexicographically stacking the mode- k_1k_2 slices of an N -way tensor into a three-way tensor, which is a three-way extension of the well-known mode- k tensor matricization. Based on it, we define a novel tensor rank, the tensor N -tubal rank, as a vector whose elements contain the tubal rank of all mode- k_1k_2 unfolding tensors, to depict the correlations along different modes. To efficiently minimize the proposed N -tubal rank, we establish its convex relaxation: the weighted sum of tensor nuclear norm (WSTNN). Then, we apply WSTNN to low-rank tensor completion (LRTC) and tensor robust principal component analysis (TRPCA). The corresponding WSTNN-based LRTC and TRPCA models are proposed, and two efficient alternating direction method of multipliers (ADMM)-based algorithms are developed to solve the proposed models. Numerical experiments demonstrate that the proposed models significantly outperform the compared ones.

Keywords: Low-rank tensor recovery (LRTR), mode- k_1k_2 tensor unfolding, the tensor N -tubal rank, the weighted sum of tensor nuclear norm (WSTNN), alternating direction method of multipliers (ADMM).

1. Introduction

As a multidimensional array, the tensor [1] plays an increasingly significant role in many applications, such as color image/video processing [2–8], hyperspectral/multispectral image (HSI/MSI) processing [9–15], background subtraction [16, 17], video rain streak removal [18–20], and magnetic resonance imaging (MRI) data recovery [21, 22]. Many of them can be formulated as the tensor recovery problem, i.e., recovering the underlying tensor from a corrupted observation tensor. Particularly, as two typical tensor recovery problems, tensor completion aims to complete missing elements, and tensor robust principal component analysis (TRPCA) aims to remove sparse outliers. The key of tensor recovery is to explore the redundancy prior of the underlying tensor, which is usually formulated as low-rankness. Thus, low-rank modeling has been widely studied and has achieved great success in tensor recovery task.

*Corresponding author. Tel.: +86 28 61831016, Fax: 86 28 61831280.

Email addresses: zhengyubang@163.com (Yu-Bang Zheng), tingzhuhuang@126.com (Ting-Zhu Huang), xlzhao122003@163.com (Xi-Le Zhao), taixiangjiang@gmail.com (Tai-Xiang Jiang), tengyu_j66@126.com (Teng-Yu Ji), nkmt0307@126.com (Tian-Hui Ma)

The traditional matrix recovery problem is actually the two-way tensor recovery problem. Since the matrix rank, measured by the number of non-zero singular values, is powerful to capture the global information of matrix, most matrix recovery methods aim to minimize the matrix rank [23–26]. However, directly minimizing the matrix rank is NP-hard [27]. To tackle this issue, the nuclear norm ($\|\cdot\|_*$), the sum of non-zero singular values, has been proposed to approximate the matrix rank, leading to great successes [23, 24].

The tensor recovery problem can be viewed as an extension of the matrix recovery problem. Inspired by the success of matrix rank minimization, it seems natural to recover the underlying tensor by minimizing the tensor rank. Mathematically, the low-rank tensor recovery (LRTR) model can be generally written as

$$\min_{\mathcal{X}} \text{rank}(\mathcal{X}) + \lambda L(\mathcal{X}, \mathcal{F}),$$

where \mathcal{X} is the underlying tensor, \mathcal{F} is the observed tensor, and $L(\mathcal{X}, \mathcal{F})$ is the loss function between \mathcal{X} and \mathcal{F} , e.g., $\mathcal{X}_\Omega = \mathcal{F}_\Omega$ for low-rank tensor completion (LRTC) and $\|\mathcal{F} - \mathcal{X}\|_1$ for TRPCA. The conclusive issue of LRTR is the definition of the tensor rank. However, unlike matrix rank, the definition of the tensor rank is not unique. Many research efforts have been devoted to defining the tensor rank, and most of them are defined based on the corresponding tensor decomposition, such as the CANDECOMP/PARAFAC (CP) rank based on the CP decomposition [28–30], the Tucker rank based on the Tucker decomposition [31–36], and the tensor tubal rank based on the tensor singular value decomposition (t-SVD) [37–39].

The CP rank and the Tucker rank are two most typical definitions of the tensor rank. The CP rank is defined as the minimum number of rank-one tensors required to express a tensor [1], i.e.,

$$\text{rank}_{\text{cp}}(\mathcal{X}) := \min \left\{ r \mid \mathcal{X} = \sum_{i=1}^r \mathbf{a}_i^1 \circ \mathbf{a}_i^2 \circ \cdots \circ \mathbf{a}_i^N, \mathbf{a}_i^k \in \mathbb{R}^{n_k} \right\},$$

where \mathcal{X} is an N -way tensor and \circ denotes the vector outer product. Although the measure of the CP rank is consistent with that of the matrix rank, it is hard to establish a solvable relaxation form for it. The Tucker rank is defined as a vector, the k -th element of which is the rank of the mode- k unfolding matrix [1], i.e.,

$$\text{rank}_{\text{tc}}(\mathcal{X}) := (\text{rank}(X_{(1)}), \text{rank}(X_{(2)}), \cdots, \text{rank}(X_{(N)})),$$

where \mathcal{X} is an N -way tensor and $X_{(k)}$ ($k = 1, 2, \dots, N$) is the mode- k unfolding of \mathcal{X} . To efficiently minimize it, Liu et al. [35] adopted the sum of the nuclear norm (SNN) of the mode- k unfolding matrix as its convex relaxation, i.e.,

$$\|\mathcal{X}\|_{\text{SNN}} := \sum_{k=1}^N \alpha_k \|X_{(k)}\|_*,$$

where $\alpha_k \geq 0$ ($k = 1, 2, \dots, N$) and $\sum_{k=1}^N \alpha_k = 1$. Based on SNN, Liu et al. [35] established a LRTC model with three solving algorithms (SiLRTC, FaLRTC, and HaLRTC), and Goldfarb and Qin [40] proposed a TRPCA model. Although SNN can flexibly exploit the correlation along each mode by adjusting the weights α_k [41], as pointed out in [37, 42], when a tensor is unfolded to a matrix along one mode, the structures information along other modes will be destroyed. Thus, SNN is difficult to preserve the intrinsic structure of the tensor.

Recently, the t-SVD and the corresponding tensor tubal rank (and multi rank) have received considerable attentions [37–39, 43–53]. As a generalization of the matrix singular value decomposition (SVD), the t-SVD regards a three-way tensor \mathcal{X} as a matrix, each element of which is a tube (mode-3 fiber), and then decomposes \mathcal{X} as

$$\mathcal{X} = \mathcal{U} * \mathcal{S} * \mathcal{V}^T,$$

where \mathcal{U} and \mathcal{V} are orthogonal tensors, \mathcal{S} is a f-diagonal tensor, \mathcal{V}^T denotes the conjugate transpose of \mathcal{V} , and $*$ denote the t-product (see details in Section 2). Mathematically, this decomposition is equivalent to a series of matrix SVDs in the Fourier domain [39], i.e.,

$$\bar{X}^{(i)} = \bar{U}^{(i)} \bar{S}^{(i)} (\bar{V}^{(i)})^T, \quad i = 1, 2, \dots, n_3,$$

where $\bar{X}^{(i)}$ is the i -th frontal slice of $\bar{\mathcal{X}}$, and $\bar{\mathcal{X}}$ is generated by performing the Discrete Fourier Transformation (DFT) along each tube of \mathcal{X} . The multi rank of \mathcal{X} is defined as a vector whose i -th element is the rank of $\bar{X}^{(i)}$, i.e.,

$$\text{rank}_m(\mathcal{X}) := (\text{rank}(\bar{X}^{(1)}), \text{rank}(\bar{X}^{(2)}), \dots, \text{rank}(\bar{X}^{(n_3)})).$$

The tubal rank of \mathcal{X} is defined as the number of non-zero tubes of \mathcal{S} , i.e.,

$$\text{rank}_t(\mathcal{X}) := \#\{i : \mathcal{S}(i, i, :) \neq 0\}.$$

Especially, the tensor tubal rank is equal to the maximum value of tensor multi rank. Since directly minimizing the tensor tubal/multi rank is NP-hard [27], Semerci et al. [53] developed a tensor nuclear norm (TNN) as their convex surrogate, i.e.,

$$\|\mathcal{X}\|_{\text{TNN}} := \sum_{i=1}^{n_3} \|\bar{X}^{(i)}\|_*.$$

Then, Zhang et al. [39, 43] proposed the TNN-based LRTC and TRPCA models, Lu et al. [46] further proved the exactly-recover-property for TNN-based TRPCA model, and Hu et al. [47] proposed a twist tensor nuclear norm (t-TNN) for the video completion.

TNN has shown its effectiveness to preserve the intrinsic structure of the tensor [39, 43, 47]. However, TNN has two obvious shortcomings, one is its inapplicability for N -way tensors ($N > 3$), and another is its inflexibility for handling different correlations along different modes, especially the third mode. Specifically, under the framework of t-SVD, for a three-way tensor, the correlations along the first and the second mode are characterized by the SVD while that along the third mode is encoded by the embedded circular convolution [39, 49]. And most of real-world data are always with different correlations along each of its modes, e.g., the correlation of a HSI along its spectral mode should be much stronger than those along its spatial modes. Thus, treating each mode flexibly like SNN is expected to compensate for this defect.

To overcome the above two issues, in this paper, we define a three-way extension of the tensor matricization operator, named mode- $k_1 k_2$ tensor unfolding ($k_1 < k_2$), as the process of lexicographically stacking the mode- $k_1 k_2$ slices of an N -way tensor $\mathcal{X} \in \mathbb{R}^{n_1 \times n_2 \times \dots \times n_N}$ into the frontal slices of a three-way tensor $\mathcal{X}_{(k_1 k_2)} \in \mathbb{R}^{n_{k_1} \times n_{k_2} \times \prod_{s \neq k_1, k_2} n_s}$ (see details in Section 3). Mathematically, the (i_1, i_2, \dots, i_N) -th element of \mathcal{X} maps to the (i_{k_1}, i_{k_2}, j) -th element of $\mathcal{X}_{(k_1 k_2)}$, where

$$j = 1 + \sum_{\substack{s=1 \\ s \neq k_1, s \neq k_2}}^N (i_s - 1) J_s \quad \text{with} \quad J_s = \prod_{\substack{m=1 \\ m \neq k_1, m \neq k_2}}^{s-1} n_m.$$

To character the correlations along different modes in a more flexible manner, we propose a new tensor rank, termed as tensor N -tubal rank, which is defined as a vector, whose elements contain the tubal rank of all mode- $k_1 k_2$ unfolding tensors, i.e.,

$$\begin{aligned} N\text{-rank}_t(\mathcal{X}) = & (\text{rank}_t(\mathcal{X}_{(12)}), \text{rank}_t(\mathcal{X}_{(13)}), \dots, \text{rank}_t(\mathcal{X}_{(1N)}), \\ & \text{rank}_t(\mathcal{X}_{(23)}), \dots, \text{rank}_t(\mathcal{X}_{(2N)}), \\ & \dots, \text{rank}_t(\mathcal{X}_{(N-1N)})) \in \mathbb{R}^{N(N-1)/2}. \end{aligned}$$

Table 1: The rank estimation of two HSIs.

Data	Size	Tucker rank	N -tubal rank
<i>Washington DC Mall</i>	$256 \times 256 \times 150$	(107,110,6)	(182,8,8)
<i>Pavia University</i>	$256 \times 256 \times 87$	(115,119,7)	(137,8,8)

Table 1 gives the rank estimation¹ of two HSIs. As observed, the rank of the mode-3 unfolding matrix is much lower than the size of the third mode, which implies a strong correlation along the third mode. According to the tensor N -tubal rank, such a strong correlation is inadequately depicted by the first element (the tubal rank), while can be exactly depicted by the other two elements. This observation from Table 1 demonstrates that compared with the tensor tubal rank, the novel tensor N -tubal rank has the advantage of flexible and simultaneous depiction for the correlations along different modes.

To efficiently minimize the proposed tensor N -tubal rank, we design its convex relaxation: the weighted sum of tensor nuclear norm (WSTNN), which can be expressed as the weighted sum of the TNN of each mode- $k_1 k_2$ unfolding tensor, i.e.,

$$\|\mathcal{X}\|_{\text{WSTNN}} := \sum_{1 \leq k_1 < k_2 \leq N} \alpha_{k_1 k_2} \|\mathcal{X}_{(k_1 k_2)}\|_{\text{TNN}},$$

where $\alpha_{k_1 k_2} \geq 0$ ($1 \leq k_1 < k_2 \leq N, k_1, k_2 \in \mathbb{Z}$) and $\sum_{1 \leq k_1 < k_2 \leq N} \alpha_{k_1 k_2} = 1$. Then, we apply the WSTNN to two typical LRTR problems, LRTC and TRPCA problems, and propose the WSTNN-based LRTC and TRPCA models. Meanwhile, two efficient alternating direction method of multipliers (ADMM)-based algorithms [54, 55] are developed to solve the proposed models. Numerous numerical experiments on synthetic and real-world data are conducted to illustrate the effectiveness and the efficiency of the proposed methods.

The rest of this paper is organized as follows. Section 2 presents some preliminary knowledge. Section 3 gives the definitions of tensor N -tubal rank and its convex surrogate WSTNN. Section 4 proposes the WSTNN-based LRTC and TRPCA models and develops two efficient ADMM-based solvers. Section 5 evaluates the performance of the proposed models and compares the results with state-of-the-art competing methods. Section 6 concludes this paper.

2. Notations and preliminaries

In this section, we give the basic notations and briefly introduce some definitions that will be used in this work [1, 39].

We denote vectors as bold lowercase letters (e.g., \mathbf{x}), matrices as uppercase letters (e.g., X), and tensors as calligraphic letters (e.g., \mathcal{X}). For a three-way tensor $\mathcal{X} \in \mathbb{R}^{n_1 \times n_2 \times n_3}$, with the MATLAB notation, we denote its (i, j, s) -th element as $\mathcal{X}(i, j, s)$ or $\mathcal{X}_{i,j,s}$, its (i, j) -th mode-1, mode-2, and mode-3 fibers as $\mathcal{X}(:, i, j)$, $\mathcal{X}(i, :, j)$, and $\mathcal{X}(i, j, :)$, respectively. We use $\mathcal{X}(i, :, :)$, $\mathcal{X}(:, i, :)$, and $\mathcal{X}(:, :, i)$ to denote the i -th horizontal, lateral, and frontal slices of \mathcal{X} , respectively. More compactly, $X^{(i)}$ is used to represent $\mathcal{X}(:, :, i)$. The Frobenius norm of \mathcal{X} is defined as $\|\mathcal{X}\|_F := (\sum_{i,j,s} |\mathcal{X}(i, j, s)|^2)^{1/2}$. The ℓ_1 norm of \mathcal{X} is defined as $\|\mathcal{X}\|_1 := \sum_{i,j,s} |\mathcal{X}(i, j, s)|$. We use $\bar{\mathcal{X}}$ to denote the tensor generated by performing DFT along each tube of \mathcal{X} , i.e., $\bar{\mathcal{X}} = \text{fft}(\mathcal{X}, [], 3)$. Naturally, we can compute \mathcal{X} via $\mathcal{X} = \text{ifft}(\bar{\mathcal{X}}, [], 3)$.

The vectorization of an N -way tensor $\mathcal{X} \in \mathbb{R}^{n_1 \times n_2 \times \dots \times n_N}$, denote as $\mathbf{x} = \text{vec}(\mathcal{X}) \in \mathbb{R}^{n_1 n_2 \dots n_N}$, is

¹The rank is approximated by the numbers of the singular values which are larger than 0.01 of the largest one.

defined as

$$\mathbf{x}(j) = \mathcal{X}(i_1, i_2, \dots, i_N) \text{ with } j = i_1 + \sum_{s=2}^N \left((i_s - 1) \prod_{m=1}^{s-1} n_m \right).$$

The mode- k tensor matricization of an N -way tensor $\mathcal{X} \in \mathbb{R}^{n_1 \times n_2 \times \dots \times n_N}$ is denoted as $X_{(k)} \in \mathbb{R}^{n_k \times \prod_{s \neq k} n_s}$, whose (i_k, j) -th element maps to the (i_1, i_2, \dots, i_N) -th element of \mathcal{X} , where

$$j = 1 + \sum_{s=1, s \neq k}^N (i_s - 1) J_s \text{ with } J_s = \prod_{m=1, m \neq k}^{s-1} n_m.$$

The corresponding operator and inverse operator is denoted as ‘‘unfold’’ and ‘‘fold’’, i.e., $X_{(k)} = \text{unfold}(\mathcal{X}, k)$ and $\mathcal{X} = \text{fold}(X_{(k)}, k)$

For a three-way tensor $\mathcal{X} \in \mathbb{R}^{n_1 \times n_2 \times n_3}$, the block circulation operation is defined as

$$\text{bcirc}(\mathcal{X}) := \begin{pmatrix} X^{(1)} & X^{(n_3)} & \dots & X^{(2)} \\ X^{(2)} & X^{(1)} & \dots & X^{(3)} \\ \vdots & \vdots & \ddots & \vdots \\ X^{(n_3)} & X^{(n_3-1)} & \dots & X^{(1)} \end{pmatrix} \in \mathbb{R}^{n_1 n_3 \times n_2 n_3}.$$

The block diagonalization operation and its inverse operation are defined as

$$\text{bdiag}(\mathcal{X}) := \begin{pmatrix} X^{(1)} & & & \\ & X^{(2)} & & \\ & & \ddots & \\ & & & X^{(n_3)} \end{pmatrix} \in \mathbb{R}^{n_1 n_3 \times n_2 n_3}, \quad \text{bdfold}(\text{bdiag}(\mathcal{X})) := \mathcal{X}.$$

The block vectorization operation and its inverse operation are defined as

$$\text{bvec}(\mathcal{X}) := ((X^{(1)})^T, (X^{(2)})^T, \dots, (X^{(n_3)})^T)^T \in \mathbb{R}^{n_1 n_3 \times n_2}, \quad \text{bvfold}(\text{bvec}(\mathcal{X})) := \mathcal{X}.$$

Definition 1 (t-product). The t-product between two three-way tensors $\mathcal{X} \in \mathbb{R}^{n_1 \times n_2 \times n_3}$ and $\mathcal{Y} \in \mathbb{R}^{n_2 \times n_4 \times n_3}$ is defined as

$$\mathcal{X} * \mathcal{Y} := \text{bvfold}(\text{bcirc}(\mathcal{X}) \text{bvec}(\mathcal{Y})) \in \mathbb{R}^{n_1 \times n_4 \times n_3}.$$

Indeed, the t-product can be regarded as a matrix-matrix multiplication, except that the multiplication operation between scalars is replaced by circular convolution between the tubes, i.e.,

$$\mathcal{F} = \mathcal{X} * \mathcal{Y} \Leftrightarrow \mathcal{F}(i, j, :) = \sum_{t=1}^{n_2} \mathcal{X}(i, t, :) \star \mathcal{Y}(t, j, :),$$

where \star denotes the circular convolution between two tubes. Note that the circular convolution in the spatial domain is equivalent to the multiplication in the Fourier domain, the t-product between two tensors $\mathcal{F} = \mathcal{X} * \mathcal{Y}$ is equivalent to

$$\bar{\mathcal{F}} = \text{bdfold}(\text{bdiag}(\bar{\mathcal{X}}) \text{bdiag}(\bar{\mathcal{Y}})).$$

Definition 2 (special tensors). The conjugate transpose of a three-way tensor $\mathcal{X} \in \mathbb{R}^{n_1 \times n_2 \times n_3}$, denote as \mathcal{X}^T , is the tensor obtained by conjugate transposing each of the frontal slices and then reversing the order of transposed frontal slices 2 through n_3 . The identity tensor $\mathcal{I} \in \mathbb{R}^{n_1 \times n_2 \times n_3}$ is the tensor whose first frontal slice is the identity matrix, and other frontal slices are all zeros. A three-way tensor \mathcal{Q} is orthogonal if $\mathcal{Q} * \mathcal{Q}^T = \mathcal{Q}^T * \mathcal{Q} = \mathcal{I}$. A three-way tensor \mathcal{S} is f-diagonal if each of its frontal slices is a diagonal matrix.

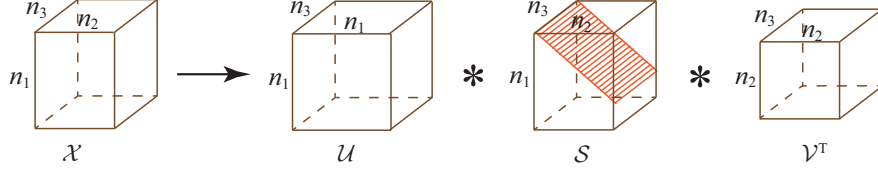


Figure 1: Illustration of the t-SVD of an $n_1 \times n_2 \times n_3$ tensor.

Algorithm 1 The t-SVD for three-way tensors

Input: $\mathcal{X} \in \mathbb{R}^{n_1 \times n_2 \times n_3}$.

- 1: $\bar{\mathcal{X}} \leftarrow \text{fft}(\mathcal{X}, [], 3)$.
- 2: **for** $i = 1$ to n_3 **do**
- 3: $[U, S, V] = \text{svd}(\bar{\mathcal{X}}^{(i)})$.
- 4: $\bar{U}^{(i)} \leftarrow U$; $\bar{S}^{(i)} \leftarrow S$; $\bar{V}^{(i)} \leftarrow V$.
- 5: **end for**
- 6: $\mathcal{U} \leftarrow \text{ifft}(\bar{U}, [], 3)$.
- 7: $\mathcal{S} \leftarrow \text{ifft}(\bar{S}, [], 3)$.
- 8: $\mathcal{V} \leftarrow \text{ifft}(\bar{V}, [], 3)$.

Output: $\mathcal{U}, \mathcal{S}, \mathcal{V}$.

Theorem 1 (t-SVD). Let $\mathcal{X} \in \mathbb{R}^{n_1 \times n_2 \times n_3}$ is a three-way tensor, then it can be factored as

$$\mathcal{X} = \mathcal{U} * \mathcal{S} * \mathcal{V}^T,$$

where $\mathcal{U} \in \mathbb{R}^{n_1 \times n_1 \times n_3}$ and $\mathcal{V} \in \mathbb{R}^{n_2 \times n_2 \times n_3}$ are the orthogonal tensors, and $\mathcal{S} \in \mathbb{R}^{n_1 \times n_2 \times n_3}$ is a f-diagonal tensor.

Fig. 1 illustrates the t-SVD scheme. The t-SVD can be efficiently obtained by computing a series of matrix SVDs in the Fourier domain; see Algorithm 1. Now, we give the definition of the corresponding tensor tubal rank and multi rank.

Definition 3 (tensor tubal rank and multi rank). Let $\mathcal{X} \in \mathbb{R}^{n_1 \times n_2 \times n_3}$ be a three-way tensor, the tensor multi rank of \mathcal{X} is a vector $\text{rank}_m(\mathcal{X}) \in \mathbb{R}^{n_3}$, whose i -th element is the rank of i -th frontal slice of $\bar{\mathcal{X}}$, where $\bar{\mathcal{X}} = \text{fft}(\mathcal{X}, [], 3)$. The tubal rank of \mathcal{X} , denote as $\text{rank}_t(\mathcal{X})$, is defined as the number of non-zero tubes of \mathcal{S} , where \mathcal{S} comes from the t-SVD of \mathcal{X} : $\mathcal{X} = \mathcal{U} * \mathcal{S} * \mathcal{V}^T$. That is, $\text{rank}_t(\mathcal{X}) = \max(\text{rank}_m(\mathcal{X}))$.

Definition 4 (tensor nuclear norm (TNN)). The tensor nuclear norm of a tensor $\mathcal{X} \in \mathbb{R}^{n_1 \times n_2 \times n_3}$, denoted as $\|\mathcal{X}\|_{\text{TNN}}$, is defined as the sum of singular values of all the frontal slices of $\bar{\mathcal{X}}$, i.e.,

$$\|\mathcal{X}\|_{\text{TNN}} := \sum_{i=1}^{n_3} \|\bar{\mathcal{X}}^{(i)}\|_*.$$

where $\bar{\mathcal{X}}^{(i)}$ is the i -th frontal slice of $\bar{\mathcal{X}}$, and $\bar{\mathcal{X}} = \text{fft}(\mathcal{X}, [], 3)$.

3. Tensor N -tubal rank and convex relaxation

In this section, we first propose the mode- $k_1 k_2$ tensor unfolding operation, then give the definitions of tensor N -tubal rank and its convex relaxation WSTNN.

Slices of a tensor are its two-dimensional sections, as the three-way tensors can be directly visualized in three-dimensional space, scholars commonly and visually denote their three kinds of slices as horizontal, lateral, and frontal slices, respectively. However, this naming method is not feasible for higher-way tensors, such as four-way tensors. Therefore, we give the following definition for the slices of N -way tensors.

Definition 5 (mode- k_1k_2 slices). The mode- k_1k_2 slices ($X^{k_1k_2}$, $1 \leq k_1 < k_2 \leq N$, $k_1, k_2 \in \mathbb{Z}$) of an N -way tensor $\mathcal{X} \in \mathbb{R}^{n_1 \times n_2 \times \dots \times n_N}$ are its two-dimensional sections, defined by fixing all but the mode- k_1 and the mode- k_2 indexes.

For example, for a four-way tensor $\mathcal{X} \in \mathbb{R}^{2 \times 3 \times 3 \times 2}$, its (i_2, i_4) -th mode-13 slice and (i_1, i_3) -th mode-24 slice are

$$X^{13} = \begin{pmatrix} \mathcal{X}(1, i_2, 1, i_4) & \mathcal{X}(1, i_2, 2, i_4) & \mathcal{X}(1, i_2, 3, i_4) \\ \mathcal{X}(2, i_2, 1, i_4) & \mathcal{X}(2, i_2, 2, i_4) & \mathcal{X}(2, i_2, 3, i_4) \end{pmatrix} \text{ and } X^{24} = \begin{pmatrix} \mathcal{X}(i_1, 1, i_3, 1) & \mathcal{X}(i_1, 1, i_3, 2) \\ \mathcal{X}(i_1, 2, i_3, 1) & \mathcal{X}(i_1, 2, i_3, 2) \\ \mathcal{X}(i_1, 3, i_3, 1) & \mathcal{X}(i_1, 3, i_3, 2) \end{pmatrix},$$

respectively. With the definition of mode- k_1k_2 slices, we define the following mode- k_1k_2 tensor unfolding.

Definition 6 (mode- k_1k_2 tensor unfolding). For an N -way tensor $\mathcal{X} \in \mathbb{R}^{n_1 \times n_2 \times \dots \times n_N}$, its mode- k_1k_2 unfolding is a three-way tensor denoted by $\mathcal{X}_{(k_1k_2)} \in \mathbb{R}^{n_{k_1} \times n_{k_2} \times \prod_{s \neq k_1, k_2} n_s}$, whose frontal slices are the lexicographic ordering of the mode- k_1k_2 slices of \mathcal{X} . Mathematically, the (i_1, i_2, \dots, i_N) -th element of \mathcal{X} maps to the (i_{k_1}, i_{k_2}, j) -th element of $\mathcal{X}_{(k_1k_2)}$, where

$$j = 1 + \sum_{\substack{s=1 \\ s \neq k_1, s \neq k_2}}^N (i_s - 1)J_s \text{ with } J_s = \prod_{\substack{m=1 \\ m \neq k_1, m \neq k_2}}^{s-1} n_m.$$

We define the corresponding operation as $\mathcal{X}_{(k_1k_2)} := \mathbf{t}\text{-unfold}(\mathcal{X}, k_1, k_2)$, and its inverse operation as $\mathcal{X} := \mathbf{t}\text{-fold}(\mathcal{X}_{(k_1k_2)}, k_1, k_2)$ ².

For example, for a four-way tensor $\mathcal{X} \in \mathbb{R}^{2 \times 3 \times 3 \times 2}$, its mode-24 unfolding tensor $\mathcal{X}_{(24)} \in \mathbb{R}^{3 \times 2 \times 6}$ can be expressed as

$$\begin{aligned} \mathcal{X}_{(24)}(:, :, 1) &= \begin{pmatrix} \mathcal{X}(1, 1, 1, 1) & \mathcal{X}(1, 1, 1, 2) \\ \mathcal{X}(1, 2, 1, 1) & \mathcal{X}(1, 2, 1, 2) \\ \mathcal{X}(1, 3, 1, 1) & \mathcal{X}(1, 3, 1, 2) \end{pmatrix}, \quad \mathcal{X}_{(24)}(:, :, 4) = \begin{pmatrix} \mathcal{X}(1, 1, 2, 1) & \mathcal{X}(1, 1, 2, 2) \\ \mathcal{X}(1, 2, 2, 1) & \mathcal{X}(1, 2, 2, 2) \\ \mathcal{X}(1, 3, 2, 1) & \mathcal{X}(1, 3, 2, 2) \end{pmatrix}, \\ \mathcal{X}_{(24)}(:, :, 2) &= \begin{pmatrix} \mathcal{X}(2, 1, 1, 1) & \mathcal{X}(2, 1, 1, 2) \\ \mathcal{X}(2, 2, 1, 1) & \mathcal{X}(2, 2, 1, 2) \\ \mathcal{X}(2, 3, 1, 1) & \mathcal{X}(2, 3, 1, 2) \end{pmatrix}, \quad \mathcal{X}_{(24)}(:, :, 5) = \begin{pmatrix} \mathcal{X}(2, 1, 2, 1) & \mathcal{X}(2, 1, 2, 2) \\ \mathcal{X}(2, 2, 2, 1) & \mathcal{X}(2, 2, 2, 2) \\ \mathcal{X}(2, 3, 2, 1) & \mathcal{X}(2, 3, 2, 2) \end{pmatrix}, \\ \mathcal{X}_{(24)}(:, :, 3) &= \begin{pmatrix} \mathcal{X}(3, 1, 1, 1) & \mathcal{X}(3, 1, 1, 2) \\ \mathcal{X}(3, 2, 1, 1) & \mathcal{X}(3, 2, 1, 2) \\ \mathcal{X}(3, 3, 1, 1) & \mathcal{X}(3, 3, 1, 2) \end{pmatrix}, \quad \mathcal{X}_{(24)}(:, :, 6) = \begin{pmatrix} \mathcal{X}(3, 1, 2, 1) & \mathcal{X}(3, 1, 2, 2) \\ \mathcal{X}(3, 2, 2, 1) & \mathcal{X}(3, 2, 2, 2) \\ \mathcal{X}(3, 3, 2, 1) & \mathcal{X}(3, 3, 2, 2) \end{pmatrix}. \end{aligned}$$

²By using the Matlab commands, we can compute $\mathcal{X}_{(k_1k_2)}$ via

$$\mathcal{X}_{(k_1k_2)} = \mathbf{reshape}(\mathbf{permute}(\mathcal{X}, [k_1, k_2, \mathbf{setdiff}([1 : N], [k_1, k_2])]), \mathbf{dim}(k_1), \mathbf{dim}(k_2), []),$$

and compute \mathcal{X} via

$$\mathcal{X} = \mathbf{ipermute}(\mathbf{reshape}(\mathcal{X}_{(k_1k_2)}, \mathbf{dim}([k_1, k_2, \mathbf{setdiff}([1 : N], [k_1, k_2])])), [k_1, k_2, \mathbf{setdiff}([1 : N], [k_1, k_2])]),$$

where $\mathbf{dim} = \mathbf{size}(\mathcal{X})$ and $N = \mathbf{ndims}(\mathcal{X})$.

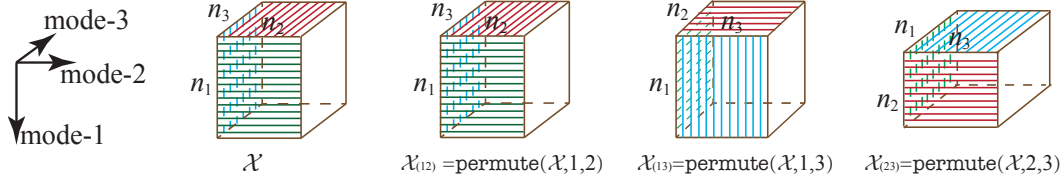


Figure 2: Illustration the permutation tensor of an $n_1 \times n_2 \times n_3$ tensor.

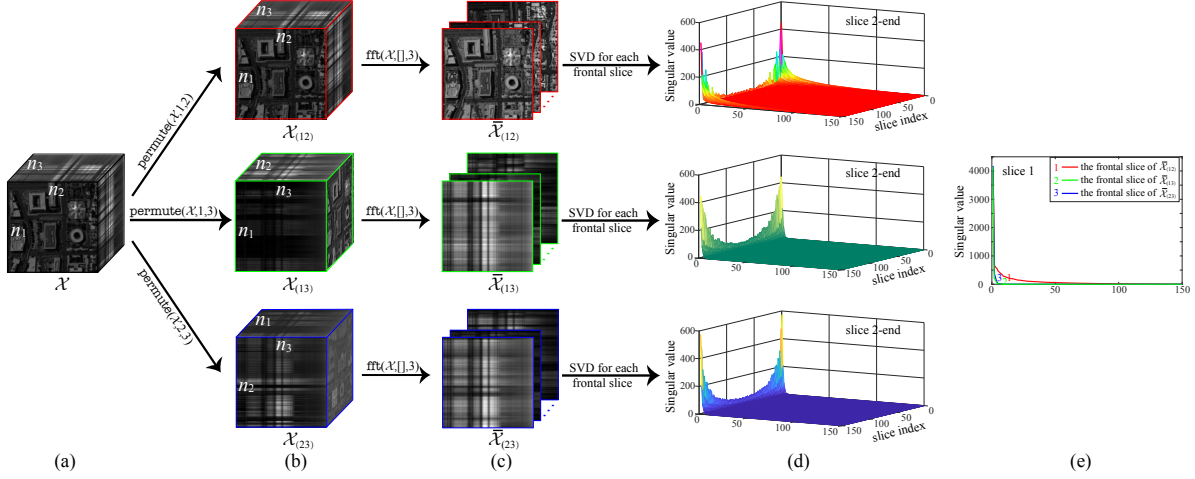


Figure 3: Illustration of the low N -tubal rank prior of a HSI. (a) The HSI *Washington DC Mall* of size $150 \times 150 \times 150$. (b) The mode- $k_1 k_2$ permutation tensors of \mathcal{X} . (c) The generated tensors $\tilde{\mathcal{X}}_{(k_1 k_2)}$ by performing the DFT along each tube of $\mathcal{X}_{(k_1 k_2)}$. (d) Singular value curves from the second to the end frontal slices of $\tilde{\mathcal{X}}_{(k_1 k_2)}$. (e) Singular value curves of the first frontal slices of $\tilde{\mathcal{X}}_{(k_1 k_2)}$.

Especially, for a three-way tensor, the proposed tensor unfolding operation does not involve dimensional-reduction, while corresponds to a permutation operation, i.e.,

$$\mathcal{X}(i, j, s) = \mathcal{X}_{(12)}(i, j, s) = \mathcal{X}_{(13)}(i, s, j) = \mathcal{X}_{(23)}(j, s, i).$$

Therefore, in this case, we use `permute` and `ipermute` to replace `t-unfold` and `t-fold`, respectively. Fig. 2 illustrates the mode- $k_1 k_2$ permutation (unfolding) tensor of an $n_1 \times n_2 \times n_3$ tensor.

As pointed out in Section 1, the framework of t-SVD and the corresponding tubal rank are applicable only to three-way tensors and lack of flexibility to handle different correlations along different modes. To handle these two issues, we perform the t-SVD on each mode- $k_1 k_2$ unfolding tensor and propose the following tensor N -tubal rank.

Definition 7 (N -tubal rank). The N -tubal rank of an N -way tensor $\mathcal{X} \in \mathbb{R}^{n_1 \times n_2 \times \dots \times n_N}$ is defined as a vector, whose elements contain the tubal rank of all mode- $k_1 k_2$ unfolding tensors, i.e.,

$$\begin{aligned} N\text{-rank}_t(\mathcal{X}) = & (\text{rank}_t(\mathcal{X}_{(12)}), \text{rank}_t(\mathcal{X}_{(13)}), \dots, \text{rank}_t(\mathcal{X}_{(1N)}), \\ & \text{rank}_t(\mathcal{X}_{(23)}), \dots, \text{rank}_t(\mathcal{X}_{(2N)}), \\ & \dots, \text{rank}_t(\mathcal{X}_{(N-1N)})) \in \mathbb{R}^{N(N-1)/2}. \end{aligned}$$

Clearly, for a three-way tensor, the tensor tubal rank is actually the first element of the tensor N -tubal rank. By taking the HSI *Washington DC Mall* shown in Fig. 3 as an example, the low N -tubal rank prior of it can be evidently observed both quantitatively and visually. Especially, the proposed N -tubal rank combines

the advantages of Tucker rank and tubal rank. On the one hand, compared with the mode- k_1 unfolding matrix, the mode- $k_1 k_2$ unfolding tensor avoids the destruction to the structures information along the k_2 -th mode. On the other hand, as shown in Fig. 3, the tubal rank of each mode- $k_1 k_2$ unfolding (permutation) tensor $\mathcal{X}_{(k_1 k_2)}$ more directly depicts the correlation of the the k_1 -th and the k_2 -th modes, i.e., it lacks of direct characterization for the correlation along other modes. As all mode- $k_1 k_2$ unfolding tensors are considered simultaneously, the proposed N -tubal rank can effectively exploit the correlations along all modes. The following theorem reveals the relationship between tensor N -tubal rank and CP rank.

Theorem 2 (N -tubal rank and CP rank). Assuming the CP rank of an N -way tensor $\mathcal{X} \in \mathbb{R}^{n_1 \times n_2 \times \dots \times n_N}$ is r , and its CP decomposition is

$$\mathcal{X} = \sum_{i=1}^r \mathbf{a}_i^1 \circ \mathbf{a}_i^2 \circ \dots \circ \mathbf{a}_i^N, \mathbf{a}_i^k \in \mathbb{R}^{n_k}, k = 1, 2, \dots, N.$$

Then the N -tubal rank of \mathcal{X} is at most $r \times \text{ones}(N(N-1)/2, 1)^3$. Especially, we define vector sets

$$\begin{aligned} \mathbb{V}_1 &= \{\mathbf{a}_i^1 | i = 1, 2, \dots, r\}, \\ \mathbb{V}_2 &= \{\mathbf{a}_i^2 | i = 1, 2, \dots, r\}, \\ &\vdots \\ \mathbb{V}_N &= \{\mathbf{a}_i^N | i = 1, 2, \dots, r\}, \end{aligned}$$

and

$$\mathbf{c}_i = \text{vec}(\mathcal{C}_i) \in \mathbb{R}^{\prod_{s \neq k_1, k_2} n_s}, i = 1, 2, \dots, r,$$

where $\mathcal{C}_i = \mathbf{a}_i^1 \circ \mathbf{a}_i^2 \circ \dots \circ \mathbf{a}_i^{k_1-1} \circ \mathbf{a}_i^{k_1+1} \circ \dots \circ \mathbf{a}_i^{k_2-1} \circ \mathbf{a}_i^{k_2+1} \circ \dots \circ \mathbf{a}_i^N$. If each vector set \mathbb{V}_i is linearly independent and each element of $\bar{\mathbf{c}}_i = \text{fft}(\mathbf{c}_i)$ is non-zero, the N -tubal rank is equal to $r \times \text{ones}(N(N-1)/2, 1)$.

Proof. The $\mathcal{X}_{(k_1 k_2)}$ has the following CP decomposition

$$\mathcal{X}_{(k_1 k_2)} = \sum_{i=1}^r \mathbf{a}_i^{k_1} \circ \mathbf{a}_i^{k_2} \circ \mathbf{c}_i,$$

Letting $\bar{\mathcal{X}}_{(k_1 k_2)} = \text{fft}(\mathcal{X}_{(k_1 k_2)}, [], 3)$, then $\bar{\mathcal{X}}_{(k_1 k_2)}$ has the the following CP decomposition

$$\bar{\mathcal{X}}_{(k_1 k_2)} = \sum_{i=1}^r \mathbf{a}_i^{k_1} \circ \mathbf{a}_i^{k_2} \circ \bar{\mathbf{c}}_i,$$

where $\bar{\mathbf{c}}_i = \text{fft}(\mathbf{c}_i)$. Letting $\bar{\mathbf{c}}_i = (\bar{c}_i^1, \bar{c}_i^2, \dots, \bar{c}_i^d)$, then the j -th frontal slice of $\bar{\mathcal{X}}_{(k_1 k_2)}$ can be expressed as

$$\bar{X}_{(k_1 k_2)}^{(j)} = \bar{c}_1^j \mathbf{a}_1^{k_1} (\mathbf{a}_1^{k_2})^T + \bar{c}_2^j \mathbf{a}_2^{k_1} (\mathbf{a}_2^{k_2})^T + \dots + \bar{c}_r^j \mathbf{a}_r^{k_1} (\mathbf{a}_r^{k_2})^T.$$

This implies that the rank of each frontal slice of $\bar{\mathcal{X}}_{(k_1 k_2)}$ is at most r , and it is equal to r if the vector sets \mathbb{V}_{k_1} or \mathbb{V}_{k_2} is linearly independent and the j -th element of each $\bar{\mathbf{c}}_i$ is non-zero. Thus, the tubal rank of $\mathcal{X}_{(k_1 k_2)}$ (the (k_1, k_2) -th element of the N -tubal rank of \mathcal{X}) is at most r , and it is equal to r if the aforementioned conditions are satisfied. \square

To effectively minimize the tensor N -tubal rank, we propose the following WSTNN as its convex relaxation.

³ $\text{ones}(n, 1) \in \mathbb{R}^n$ is a vector whose elements are all 1.

Definition 8 (the weighted sum of tensor nuclear norm). The weighted sum of tensor nuclear norm (WSTNN) of an N -way tensor $\mathcal{X} \in \mathbb{R}^{n_1 \times n_2 \times \dots \times n_N}$, denote as $\|\mathcal{X}\|_{\text{WSTNN}}$, is defined as the weighted sum of the TNN of each mode- $k_1 k_2$ unfolding tensor, i.e.,

$$\|\mathcal{X}\|_{\text{WSTNN}} := \sum_{1 \leq k_1 < k_2 \leq N} \alpha_{k_1 k_2} \|\mathcal{X}_{(k_1 k_2)}\|_{\text{TNN}},$$

where $\alpha_{k_1 k_2} \geq 0$ ($1 \leq k_1 < k_2 \leq N, k_1, k_2 \in \mathbb{Z}$) and $\sum_{1 \leq k_1 < k_2 \leq N} \alpha_{k_1 k_2} = 1$.

The weight $\alpha = (\alpha_{11}, \alpha_{12}, \dots, \alpha_{1N}, \alpha_{23}, \dots, \alpha_{2N}, \dots, \alpha_{N-1N})$ is an important parameter for WSTNN. For the choice of the weight α , we consider the following three cases.

Case 1: The tensor N -tubal rank of the underlying tensor is unknown and can not estimated empirically, such as the MRI data, the weight α is chosen to be

$$\alpha = \frac{(1, 1, \dots, 1)}{N(N-1)/2} = \frac{2(1, 1, \dots, 1)}{N(N-1)}.$$

Case 2: The tensor N -tubal rank of the underlying tensor $\mathcal{X} \in \mathbb{R}^{n_1 \times n_2 \times \dots \times n_N}$ is known, i.e.,

$$N\text{-rank}_t(\mathcal{X}) = (r_{11}, r_{12}, \dots, r_{1N}, r_{23}, \dots, r_{2N}, \dots, r_{N-1N}).$$

Since $\alpha_{k_1 k_2}$ stands for the contribution of the TNN of the mode- $k_1 k_2$ unfolding tensor $\mathcal{X}_{(k_1 k_2)}$, the value of $\alpha_{k_1 k_2}$ should be dependent on the tubal rank of $\mathcal{X}_{(k_1 k_2)}$ ($r_{k_1 k_2}$) and the size of the first two modes of $\mathcal{X}_{(k_1 k_2)}$ (n_{k_1} and n_{k_2}). Specially, larger (or smaller) ratio of $r_{k_1 k_2}$ to $\min(n_{k_1}, n_{k_2})$ corresponds to smaller (or larger) value of $\alpha_{k_1 k_2}$. Therefore, the following strategy is considered to choose the weight α , i.e.,

$$\alpha_{k_1 k_2} = \frac{e^{\frac{\eta \hat{r}_{k_1 k_2}}{R}}}{\sum_{1 \leq k_1 < k_2 \leq N} e^{\frac{\eta \hat{r}_{k_1 k_2}}{R}}}, \text{ with } R = \sum_{1 \leq k_1 < k_2 \leq N} \hat{r}_{k_1 k_2}, \quad 1 \leq k_1 < k_2 \leq N, k_1, k_2 \in \mathbb{Z},$$

where $\hat{r}_{k_1 k_2} = \frac{\min(n_{k_1}, n_{k_2}) - r_{k_1 k_2}}{\min(n_{k_1}, n_{k_2})}$ and η is a balance parameter.

Case 3: Particularly, for HSIs/MSIs, although their exact N -tubal rank is unknown, the correlation along their spectral mode should be much stronger than those along their spatial modes. It implies that the value of the first element of the N -tubal rank should be much larger than the values of the second and the third elements of it. Thus, in this case, we empirically choose the weights α as $(\theta, 1, 1)/(2 + \theta)$, and θ is a balance parameter.

4. WSTNN-based models and solving algorithms

In this section, we apply WSTNN to LRTC and TRPCA problems, and propose the WSTNN-based LRTC and WSTNN-based TRPCA models with ADMM-based solving schemes.

4.1. WSTNN-based LRTC model

Tensor completion aims at estimating the missing elements from an incomplete observation tensor. Considering an N -way tensor $\mathcal{X} \in \mathbb{R}^{n_1 \times n_2 \times \dots \times n_N}$, the proposed WSTNN-based LRTC model is formulated as

$$\begin{aligned} \min_{\mathcal{X}} \quad & \|\mathcal{X}\|_{\text{WSTNN}} \\ \text{s.t.} \quad & \mathcal{P}_\Omega(\mathcal{X} - \mathcal{F}) = 0, \end{aligned} \tag{1}$$

where \mathcal{X} is the underlying tensor, \mathcal{F} is the observed tensor, Ω is the index set for the known entries, and $\mathcal{P}_\Omega(\mathcal{X})$ is the projection operator that keeps the entries of \mathcal{X} in Ω and sets others to zero. Let

$$\iota_{\mathbb{S}}(\mathcal{X}) := \begin{cases} 0, & \text{if } \mathcal{X} \in \mathbb{S}, \\ \infty, & \text{otherwise,} \end{cases} \quad (2)$$

where $\mathbb{S} := \{\mathcal{X} \in \mathbb{R}^{n_1 \times n_2 \times \dots \times n_N}, \mathcal{P}_\Omega(\mathcal{X} - \mathcal{F}) = 0\}$. Then (1) can be rewritten as

$$\min_{\mathcal{X}} \sum_{1 \leq k_1 < k_2 \leq N} \alpha_{k_1 k_2} \|\mathcal{X}_{(k_1 k_2)}\|_{\text{TNN}} + \iota_{\mathbb{S}}(\mathcal{X}), \quad (3)$$

where $\alpha_{k_1 k_2} \geq 0$ ($1 \leq k_1 < k_2 \leq N, k_1, k_2 \in \mathbb{Z}$) and $\sum_{1 \leq k_1 < k_2 \leq N} \alpha_{k_1 k_2} = 1$.

Next, we use ADMM to solve (3). We rewrite (3) as the following equivalent constrained problem

$$\begin{aligned} \min_{\mathcal{X}, \mathcal{Y}_{k_1 k_2}} \quad & \sum_{1 \leq k_1 < k_2 \leq N} \alpha_{k_1 k_2} \|(\mathcal{Y}_{k_1 k_2})_{(k_1 k_2)}\|_{\text{TNN}} + \iota_{\mathbb{S}}(\mathcal{X}) \\ \text{s.t.} \quad & \mathcal{X} - \mathcal{Y}_{k_1 k_2} = 0, \quad 1 \leq k_1 < k_2 \leq N, k_1, k_2 \in \mathbb{Z}. \end{aligned} \quad (4)$$

The concise form of the augmented Lagrangian function of (4) can be expressed as

$$\begin{aligned} L_{\beta_{k_1 k_2}}(\mathcal{Y}_{k_1 k_2}, \mathcal{X}, \mathcal{M}_{k_1 k_2}) = \quad & \sum_{1 \leq k_1 < k_2 \leq N} \left\{ \alpha_{k_1 k_2} \|(\mathcal{Y}_{k_1 k_2})_{(k_1 k_2)}\|_{\text{TNN}} \right. \\ & \left. + \frac{\beta_{k_1 k_2}}{2} \left\| \mathcal{X} - \mathcal{Y}_{k_1 k_2} + \frac{\mathcal{M}_{k_1 k_2}}{\beta_{k_1 k_2}} \right\|_F^2 \right\} + \iota_{\mathbb{S}}(\mathcal{X}) + \mathcal{C}, \end{aligned} \quad (5)$$

where $\mathcal{M}_{k_1 k_2}$ ($1 \leq k_1 < k_2 \leq N, k_1, k_2 \in \mathbb{Z}$) are the Lagrange multipliers, $\beta_{k_1 k_2}$ ($1 \leq k_1 < k_2 \leq N, k_1, k_2 \in \mathbb{Z}$) are the penalty parameters, and \mathcal{C} is a variable, which is independent of \mathcal{X} and $\mathcal{Y}_{k_1 k_2}$. Within the framework of ADMM, $\mathcal{Y}_{k_1 k_2}$, \mathcal{X} , and $\mathcal{M}_{k_1 k_2}$ are alternately updated as

$$\begin{cases} \text{Step 1 : } \mathcal{Y}_{k_1 k_2}^{(p+1)} = \arg \min_{\mathcal{Y}_{k_1 k_2}} L_{\beta_{k_1 k_2}}(\mathcal{Y}_{k_1 k_2}, \mathcal{X}^{(p)}, \mathcal{M}_{k_1 k_2}^{(p)}), \\ \text{Step 2 : } \mathcal{X}^{(p+1)} = \arg \min_{\mathcal{X}} L_{\beta_{k_1 k_2}}(\mathcal{Y}_{k_1 k_2}^{(p+1)}, \mathcal{X}, \mathcal{M}_{k_1 k_2}^{(p)}), \\ \text{Step 3 : } \mathcal{M}_{k_1 k_2}^{(p+1)} = \mathcal{M}_{k_1 k_2}^{(p)} + \beta_{k_1 k_2}(\mathcal{X}^{(p+1)} - \mathcal{Y}_{k_1 k_2}^{(p+1)}). \end{cases} \quad (6)$$

In Step 1, the $\mathcal{Y}_{k_1 k_2}$ ($1 \leq k_1 < k_2 \leq N, k_1, k_2 \in \mathbb{Z}$) subproblems are

$$\begin{aligned} \mathcal{Y}_{k_1 k_2}^{(p+1)} = \arg \min_{\mathcal{Y}_{k_1 k_2}} \quad & \alpha_{k_1 k_2} \|(\mathcal{Y}_{k_1 k_2})_{(k_1 k_2)}\|_{\text{TNN}} \\ & + \frac{\beta_{k_1 k_2}}{2} \left\| (\mathcal{X}_{(k_1 k_2)})^{(p)} - (\mathcal{Y}_{k_1 k_2})_{(k_1 k_2)} + \frac{((\mathcal{M}_{k_1 k_2})_{(k_1 k_2)})^{(p)}}{\beta_{k_1 k_2}} \right\|_F^2. \end{aligned} \quad (7)$$

To solve (7), we introduce the following theorem [39].

Theorem 3. Assuming that $\mathcal{Z} \in \mathbb{R}^{n_1 \times n_2 \times n_3}$ is a three-way tensor, a minimizer to

$$\min_{\mathcal{Y}} \tau \|\mathcal{Y}\|_{\text{TNN}} + \frac{1}{2} \|\mathcal{Y} - \mathcal{Z}\|_F^2,$$

is given by the tensor singular value thresholding (t-SVT)

$$\mathcal{Y} = \mathcal{D}_\tau(\mathcal{Z}) := \mathcal{U} * \mathcal{S}_\tau * \mathcal{V}^T,$$

Algorithm 2 ADMM-based optimization algorithm for the proposed WSTNN-based LRTC model (1).

Input: The observed tensor \mathcal{F} , index set Ω , weight $\alpha = (\alpha_{11}, \alpha_{12}, \dots, \alpha_{1N}, \alpha_{23}, \dots, \alpha_{2N}, \dots, \alpha_{N-1N})$, $\beta = (\beta_{11}, \beta_{12}, \dots, \beta_{1N}, \beta_{23}, \dots, \beta_{2N}, \dots, \beta_{N-1N})$, $\beta_{\max} = (10^{10}, 10^{10}, \dots, 10^{10})$, and $\gamma = 1.1$.

Initialization: $\mathcal{X}_{\Omega}^{(0)} = \mathcal{F}_{\Omega}$, $\mathcal{X}_{\Omega^c}^{(0)} = 0$, $\mathcal{Y}_{k_1 k_2}^{(0)} = 0$, $\mathcal{M}_{k_1 k_2}^{(0)} = 0$, $p = 0$, and $p_{\max} = 500$.

- 1: **while** not converged and $p < p_{\max}$ **do**
- 2: Update $\mathcal{Y}_{k_1 k_2}^{(p+1)}$ via (8), $1 \leq k_1 < k_2 \leq N$, $k_1, k_2 \in \mathbb{Z}$.
- 3: Update $\mathcal{X}^{(p+1)}$ via (10).
- 4: Update $\mathcal{M}_{k_1 k_2}^{(p+1)}$ via (6), $1 \leq k_1 < k_2 \leq N$, $k_1, k_2 \in \mathbb{Z}$.
- 5: $\beta = \min(\gamma\beta, \beta_{\max})$ and $p = p + 1$.
- 6: **end while**

Output: The completed tensor \mathcal{X} .

where $\mathcal{Z} = \mathcal{U} * \mathcal{S} * \mathcal{V}^T$ and \mathcal{S}_{τ} is an $n_1 \times n_2 \times n_3$ tensor which satisfies

$$\bar{\mathcal{S}}_{\tau}(i, i, s) = \max(\bar{\mathcal{S}}(i, i, s) - \tau, 0),$$

where $\bar{\mathcal{S}} = \text{fft}(\mathcal{S}, [], 3)$, and τ is a threshold.

Via Theorem 3, \mathcal{Y}_k ($1 \leq k_1 < k_2 \leq N$, $k_1, k_2 \in \mathbb{Z}$) can be updated as

$$\mathcal{Y}_{k_1 k_2}^{(p+1)} = \text{t-fold} \left(\mathcal{D}_{\frac{\alpha_{k_1 k_2}}{\beta_{k_1 k_2}}} \left((\mathcal{X}_{(k_1 k_2)})^{(p)} + \frac{((\mathcal{M}_{k_1 k_2})^{(k_1 k_2)})^{(p)}}{\beta_{k_1 k_2}} \right), k_1, k_2 \right). \quad (8)$$

In Step 2, we solve the following problem

$$\mathcal{X}^{(p+1)} \in \arg \min_{\mathcal{X}} \sum_{1 \leq k_1 < k_2 \leq N} \frac{\beta_{k_1 k_2}}{2} \left\| \mathcal{X} - \mathcal{Y}_{k_1 k_2}^{(p+1)} + \frac{\mathcal{M}_{k_1 k_2}^{(p)}}{\beta_{k_1 k_2}} \right\|_F^2 + \iota_{\mathbb{S}}(\mathcal{X}), \quad (9)$$

which is differentiable and has a closed-form solution

$$\mathcal{X}^{(p+1)} = \mathcal{P}_{\Omega^c} \left(\frac{\sum_{1 \leq k_1 < k_2 \leq N} \beta_{k_1 k_2} (\mathcal{Y}_{k_1 k_2}^{(p+1)} - \frac{\mathcal{M}_{k_1 k_2}^{(p)}}{\beta_{k_1 k_2}})}{\sum_{1 \leq k_1 < k_2 \leq N} \beta_{k_1 k_2}} \right) + \mathcal{P}_{\Omega}(\mathcal{F}). \quad (10)$$

The pseudocode of the developed algorithm is described in Algorithm 2. The computational cost at each iteration is

$$\mathcal{O} \left(D \sum_{1 \leq k_1 < k_2 \leq N} \left(\log(d_{k_1 k_2}) + \min(n_{k_1}, n_{k_2}) \right) \right),$$

where $D = \prod_{k=1}^N n_k$ and $d_{k_1 k_2} = D / (n_{k_1} n_{k_2})$.

4.2. WSTNN-based TRPCA model

The TRPCA aims to exactly recover a low-rank tensor corrupted by sparse noise. Considering an N -way tensor $\mathcal{X} \in \mathbb{R}^{n_1 \times n_2 \times \dots \times n_N}$, the proposed WSTNN-based TRPCA model can be formulated as

$$\begin{aligned} \min_{\mathcal{L}, \mathcal{E}} \quad & \|\mathcal{L}\|_{\text{WSTNN}} + \lambda \|\mathcal{E}\|_1 \\ \text{s.t.} \quad & \mathcal{X} = \mathcal{L} + \mathcal{E}, \end{aligned} \quad (11)$$

where \mathcal{X} is the corrupted observation tensor, \mathcal{L} is the low-rank component, \mathcal{E} is the sparse component, and λ is a tuning parameter compromising \mathcal{L} and \mathcal{E} . And (11) can be rewritten as

$$\begin{aligned} \min_{\mathcal{L}, \mathcal{E}} \quad & \sum_{1 \leq k_1 < k_2 \leq N} \alpha_{k_1 k_2} \|\mathcal{L}_{(k_1 k_2)}\|_{\text{TNN}} + \lambda \|\mathcal{E}\|_1 \\ \text{s.t.} \quad & \mathcal{X} = \mathcal{L} + \mathcal{E}. \end{aligned} \quad (12)$$

where $\alpha_{k_1 k_2} \geq 0$ ($1 \leq k_1 < k_2 \leq N, k_1, k_2 \in \mathbb{Z}$) and $\sum_{1 \leq k_1 < k_2 \leq N} \alpha_{k_1 k_2} = 1$.

Next, we use ADMM to solve (12). We rewrite (12) as

$$\begin{aligned} \min_{\mathcal{L}, \mathcal{E}, \mathcal{Z}_{k_1 k_2}} \quad & \sum_{1 \leq k_1 < k_2 \leq N} \alpha_{k_1 k_2} \|(\mathcal{Z}_{k_1 k_2})_{(k_1 k_2)}\|_{\text{TNN}} + \lambda \|\mathcal{E}\|_1 \\ \text{s.t.} \quad & \mathcal{X} = \mathcal{L} + \mathcal{E}, \\ & \mathcal{L} - \mathcal{Z}_{k_1 k_2} = 0, 1 \leq k_1 < k_2 \leq N, k_1, k_2 \in \mathbb{Z}. \end{aligned} \quad (13)$$

The concise form of the augmented Lagrangian function of (13) can be expressed as

$$\begin{aligned} L_{\beta_{k_1 k_2}, \rho}(\mathcal{L}, \mathcal{Z}_{k_1 k_2}, \mathcal{P}_{k_1 k_2}, \mathcal{E}, \mathcal{M}) = & \sum_{1 \leq k_1 < k_2 \leq N} \left\{ \alpha_{k_1 k_2} \|(\mathcal{Z}_{k_1 k_2})_{(k_1 k_2)}\|_{\text{TNN}} \right. \\ & \left. + \frac{\beta_{k_1 k_2}}{2} \left\| \mathcal{L} - \mathcal{Z}_{k_1 k_2} + \frac{\mathcal{P}_{k_1 k_2}}{\beta_{k_1 k_2}} \right\|_F^2 \right\} + \lambda \|\mathcal{E}\|_1 + \frac{\rho}{2} \left\| \mathcal{X} - \mathcal{L} - \mathcal{E} + \frac{\mathcal{M}}{\rho} \right\|_F^2 + \mathcal{C}, \end{aligned} \quad (14)$$

where $\mathcal{P}_{k_1 k_2}$ and \mathcal{M} are the Lagrange multipliers, $\beta_{k_1 k_2}$ and ρ are the penalty parameters, and \mathcal{C} is a variable, which is independent of \mathcal{L} and \mathcal{E} , and $\mathcal{Z}_{k_1 k_2}$. To minimize (14), we can update $\mathcal{L}, \mathcal{Z}_{k_1 k_2}, \mathcal{P}_{k_1 k_2}, \mathcal{E}, \mathcal{M}$ ($1 \leq k_1 < k_2 \leq N, k_1, k_2 \in \mathbb{Z}$) as

$$\begin{cases} \text{Step 1 : } \mathcal{Z}_{k_1 k_2}^{(p+1)} = \arg \min_{\mathcal{Z}_{k_1 k_2}} L_{\beta_{k_1 k_2}, \rho}(\mathcal{L}^{(p)}, \mathcal{Z}_{k_1 k_2}, \mathcal{P}_{k_1 k_2}^{(p)}, \mathcal{E}^{(p)}, \mathcal{M}^{(p)}), \\ \text{Step 2 : } \mathcal{L}^{(p+1)} = \arg \min_{\mathcal{L}} L_{\beta_{k_1 k_2}, \rho}(\mathcal{L}, \mathcal{Z}_{k_1 k_2}^{(p+1)}, \mathcal{P}_{k_1 k_2}^{(p)}, \mathcal{E}^{(p)}, \mathcal{M}^{(p)}), \\ \text{Step 3 : } \mathcal{E}^{(p+1)} = \arg \min_{\mathcal{E}} L_{\beta_{k_1 k_2}, \rho}(\mathcal{L}^{(p+1)}, \mathcal{Z}_{k_1 k_2}^{(p+1)}, \mathcal{P}_{k_1 k_2}^{(p)}, \mathcal{E}, \mathcal{M}^{(p)}), \\ \text{Step 4 : } \mathcal{P}_{k_1 k_2}^{(p+1)} = \mathcal{P}_{k_1 k_2}^{(p)} + \beta_{k_1 k_2} (\mathcal{L}^{(p+1)} - \mathcal{Z}_{k_1 k_2}^{(p+1)}), \\ \text{Step 5 : } \mathcal{M}^{(p+1)} = \mathcal{M}^{(p)} + \rho (\mathcal{X} - \mathcal{L}^{(p+1)} - \mathcal{E}^{(p+1)}). \end{cases} \quad (15)$$

In Step 1, the $\mathcal{Z}_{k_1 k_2}$ ($1 \leq k_1 < k_2 \leq N, k_1, k_2 \in \mathbb{Z}$) subproblem can be solved as

$$\mathcal{Z}_{k_1 k_2}^{(p+1)} = \text{t-fold} \left(\mathcal{D}_{\frac{\alpha_{k_1 k_2}}{\beta_{k_1 k_2}}} \left((\mathcal{L}_{(k_1 k_2)})^{(p)} + \frac{((\mathcal{P}_{k_1 k_2})_{(k_1 k_2)})^{(p)}}{\beta_{k_1 k_2}} \right), k_1, k_2 \right). \quad (16)$$

In Step 2, the \mathcal{L} subproblem has the following closed-form solution

$$\mathcal{L}^{(p+1)} = \frac{\rho \left(\mathcal{X} - \mathcal{E}^{(p)} + \frac{\mathcal{M}^{(p)}}{\rho} \right) + \sum_{1 \leq k_1 < k_2 \leq N} \beta_{k_1 k_2} \left(\mathcal{Z}_{k_1 k_2}^{(p+1)} - \frac{\mathcal{P}_{k_1 k_2}^{(p)}}{\beta_{k_1 k_2}} \right)}{\rho + \sum_{1 \leq k_1 < k_2 \leq N} \beta_{k_1 k_2}}. \quad (17)$$

In Step 3, we solve the following problem

$$\mathcal{E}^{(p+1)} \in \arg \min_{\mathcal{E}} \lambda \|\mathcal{E}\|_1 + \frac{\rho}{2} \left\| \mathcal{X} - \mathcal{L}^{(p+1)} - \mathcal{E} + \frac{\mathcal{M}^{(p)}}{\rho} \right\|_F^2, \quad (18)$$

Algorithm 3 ADMM-based optimization algorithm for the proposed WSTNN-based TRPCA model (11).

Input: The corrupted observation tensor \mathcal{X} , weight $\alpha = (\alpha_{11}, \alpha_{12}, \dots, \alpha_{1N}, \alpha_{23}, \dots, \alpha_{2N}, \dots, \alpha_{N-1N})$, $\beta = (\beta_{11}, \beta_{12}, \dots, \beta_{1N}, \beta_{23}, \dots, \beta_{2N}, \dots, \beta_{N-1N})$, $\beta_{\max} = (10^{10}, 10^{10}, \dots, 10^{10})$, $\lambda, \rho, \rho_{\max} = 10^{10}$, and $\gamma = 1.2$.

- 1: Initialization: $\mathcal{L}^{(0)} = 0, \mathcal{E}^{(0)} = 0, \mathcal{M}^{(0)} = 0, \mathcal{Z}_{k_1 k_2}^{(0)} = 0, \mathcal{P}_{k_1 k_2}^{(0)} = 0$, and $p_{\max} = 500$.
- 2: **while** not converged and $p < p_{\max}$ **do**
- 3: Update $\mathcal{Z}_{k_1 k_2}^{(p+1)}$ via (16), $1 \leq k_1 < k_2 \leq N$.
- 4: Update $\mathcal{L}^{(p+1)}$ via (17).
- 5: Update $\mathcal{E}^{(p+1)}$ via (19).
- 6: Update $\mathcal{P}_{k_1 k_2}^{(p+1)}$ via (15), $1 \leq k_1 < k_2 \leq N$.
- 7: Update $\mathcal{M}^{(p+1)}$ via (15).
- 8: $\beta = \min(\gamma\beta, \beta_{\max}), \rho = \min(\gamma\rho, \rho_{\max})$, and $p = p + 1$.
- 9: **end while**

Output: The low-rank component \mathcal{L} and the sparse component \mathcal{E} .

which has the following closed-form solution

$$\mathcal{E}^{(p+1)} = \mathcal{S}_{\frac{\lambda}{\rho}} \left(\mathcal{X} - \mathcal{L}^{(p+1)} + \frac{\mathcal{M}^{(p)}}{\rho} \right), \quad (19)$$

where $\mathcal{S}_{\xi}(\cdot)$ is the tensor soft thresholding operator with threshold ξ , i.e.,

$$[\mathcal{S}_{\xi}(\mathcal{X})]_{i_1 i_2 \dots i_N} = \text{sgn}(x_{i_1 i_2 \dots i_N}) \max(|x_{i_1 i_2 \dots i_N}| - \xi, 0). \quad (20)$$

The pseudocode of the proposed algorithm to solve the proposed WSTNN-based TRPCA model (11) is described in Algorithm 3. The computational cost at each iteration is

$$\mathcal{O} \left(D \sum_{1 \leq k_1 < k_2 \leq N} \left(\log(d_{k_1 k_2}) + \min(n_{k_1}, n_{k_2}) \right) \right),$$

where $D = \prod_{k=1}^N n_k$ and $d_{k_1 k_2} = D / (n_{k_1} n_{k_2})$.

5. Numerical experiments

We evaluate the performance of the proposed WSTNN-based LRTC and TRPCA methods. Both synthetic and real-world data are tested. We employ the peak signal to noise rate (PSNR), the structural similarity (SSIM) [56], and the feature similarity (FSIM) [57] to measure the quality of the recovered results. All of them are positive indexes, i.e., the higher value, the better quality. All tests are implemented on the platform of Windows 7 and MATLAB (R2017b) with an Intel Core i5-4590 3.30GHz and 16GB RAM.

5.1. Low-rank tensor completion

In this section, we test both synthetic data and five kinds of real-world data: MSI, HSI, MRI, color video (CV), and hyperspectral video (HSV). If not specified, the methodology for sampling the data is purely random sampling. The compared LRTC methods include: HaLRTC [35] and LRTC-TVI [36], representing state-of-the-arts for Tucker decomposition based method; BCPF [30], representing state-of-the-arts for CP decomposition based method; logDet [38], TNN [39], PSTNN [44], and t-TNN [47], representing state-of-the-arts for t-SVD based method. In all four-way tensors tests, as logDet, TNN, PSTNN, and t-TNN, are

Table 2: Parameters setting in the proposed WSTNN-based LRTC method on different data.

Test	Data	α	τ
synthetic data completion	three-way tensor	(1,1,1)/3	(10,10,10)
	four-way tensor	(1,1,1,1,1,1)/6	(50,50,50,50,50,50)
real-world data completion	three-way tensor	HSI/MSI MRI	(100,100,100)
	four-way tensor	CV HSV	(500,500,500,500,500,500)

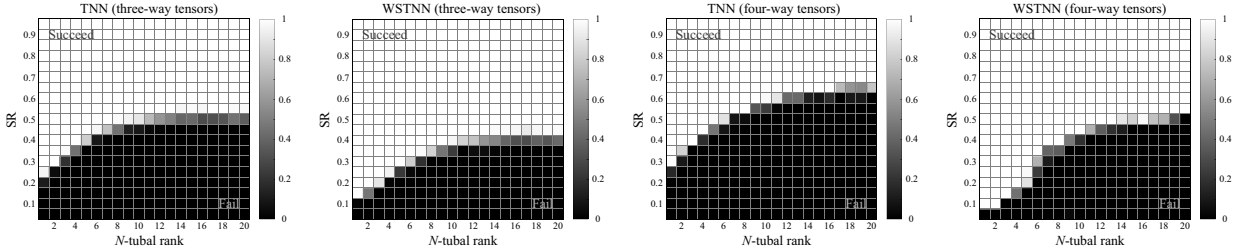


Figure 4: The success rates for synthetic data with varying N -tubal rank and varying SRs. The left two are the results of TNN-based LRTC method [39] and the proposed WSTNN-based LRTC method on three-way tensors. The right two are the results of TNN-based LRTC method [39] and the proposed WSTNN-based LRTC method on four-way tensors. The gray magnitude represents the success rates.

applicable only to three-way tensors, we first reshape the four-way tensors into three-way tensors, and then perform them.

Parameter selection. In all tests, the stopping criterion lies on the relative change (RelCha) of two successive recovered tensors, i.e., $\text{RelCha} = \frac{\|\mathcal{X}^{(p+1)} - \mathcal{X}^{(p)}\|_F}{\|\mathcal{X}^{(p)}\|_F} < 10^{-4}$. Letting the threshold parameter $\tau = \alpha/\beta$, then α is chosen by the strategy of the weight selection in Section 3, τ is set to be $\omega \times \text{ones}(N(N-1)/2, 1)^3$, and ω is empirically selected from a candidate set: $\{1, 10, 50, 100, 500, 1000, 10000\}$. Table 2 shows the parameters setting in the proposed WSTNN-based LRTC method on different data.

Synthetic data completion. We test both synthetic three-way tensors of size $30 \times 30 \times 30$ and four-way tensors of size $30 \times 30 \times 30 \times 30$. The testing synthetic tensors are consisted by the sum of r rank-one tensors, which are generated by performing vector outer product on N ($N = 3$ or 4) random vectors. In practice, the data in each test is regenerated and is confirmed to meet the conditions in Theorem 2, i.e., its N -tubal rank is $r \times \text{ones}(N(N-1)/2, 1)$. We define the success rate as the ratio of successful times to the total number of times, and one test is successful if the relative square error of the recovered tensor $\hat{\mathcal{X}}$ and the ground truth tensor \mathcal{X} , i.e. $\|\hat{\mathcal{X}} - \mathcal{X}\|_F^2 / \|\mathcal{X}\|_F^2$, is less than 10^{-3} .

We test data with different N -tubal rank and the sampling rates (SRs), which is defined as the proportion of the known elements. The N -tubal rank are set to be $r \times \text{ones}(N(N-1)/2, 1)$ ($r = 1, 2, \dots, 20$) and the SRs are set to be $0.05 \times s$ ($s = 1, 2, \dots, 19$). For each pair of N -tubal rank and SR, we conduct 50 independent tests and calculate the success rate. Fig. 4 shows the success rates for varying N -tubal rank and varying SRs, and the results demonstrate that the proposed WSTNN-based LRTC method is more robust and preferable than the TNN-based method [39].

MSI completion. We test 32 MSIs in the dataset CAVE⁴. All testing data are of size $256 \times 256 \times 31$. Table 3 lists the mean values of PSNR, SSIM, and FSIM of all 32 MSIs recovered by different LRTC

⁴<http://www.cs.columbia.edu/CAVE/databases/multispectral>.

Table 3: The average PSNR, SSIM, and FSIM values of all testing 32 MSIs by eight utilized LRTC methods.

SR	5%			10%			20%			Time(s)
Method	PSNR	SSIM	FSIM	PSNR	SSIM	FSIM	PSNR	SSIM	FSIM	
HaLRTC	14.90	0.242	0.648	21.43	0.537	0.773	32.90	0.892	0.933	13.64
LRTC-TVI	23.92	0.718	0.812	29.21	0.868	0.895	34.17	0.941	0.953	472.3
BCPF	30.47	0.785	0.884	35.66	0.903	0.936	39.62	0.944	0.962	642.7
logDet	16.99	0.309	0.679	31.27	0.780	0.894	40.81	0.968	0.977	46.31
TNN	17.64	0.332	0.692	30.90	0.780	0.894	39.60	0.962	0.974	46.14
PSTNN	19.56	0.264	0.526	32.95	0.809	0.882	40.77	0.962	0.973	63.48
t-TNN	28.32	0.779	0.874	35.45	0.942	0.954	42.67	0.985	0.987	24.79
WSTNN	32.03	0.881	0.930	38.74	0.977	0.979	45.70	0.994	0.994	75.31

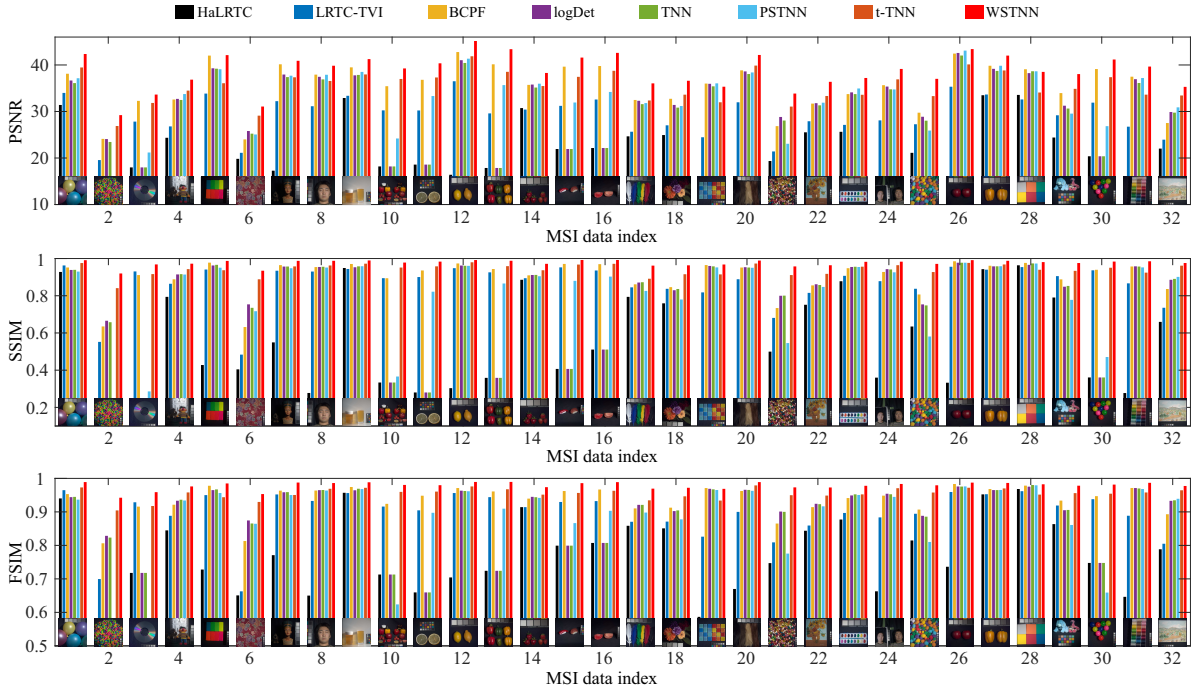


Figure 5: The PSNR, SSIM, and FSIM values of all 32 testing MSIs in the dataset CAVE output by eight utilized LRTC methods with SR = 10%.

methods. As observed, the proposed method can significantly outperform the compared methods in terms of all evaluation indices. In Fig. 5, we show the PSNR, SSIM, and FSIM values of each MSI output by eight utilized LRTC methods with SR = 10%. We can see that in all cases, the proposed method has an overall better performance than the compared ones with respect to all evaluation indices. To illustrate the visual quality, in Fig. 6, we show one band in four testing data recovered by different methods with SR = 10%. It is obvious that the proposed method is evidently superior to the compared ones, in recovery of both abundant shape structure and texture information.

HSI completion. We test HSIs *Washington DC Mall*⁵ and *Pavia University*⁵. Table 4 lists the values of PSNR, SSIM, and FSIM of these two testing HSIs recovered by different LRTC methods. We observe that compared with other methods, the proposed method consistently achieves the highest values in terms of all evaluation indexes, e.g., when SR is set as 5% or 10%, the proposed method achieves around 7 dB gain in

⁵<http://lesun.weebly.com/hyperspectral-data-set.html>.

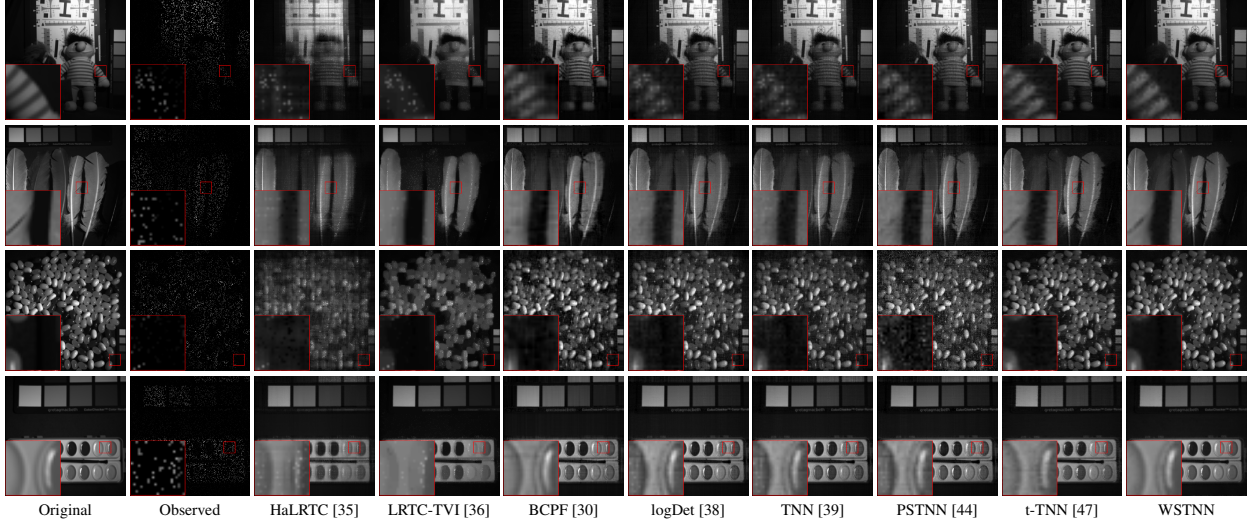


Figure 6: The completion results of four selected MSIs with $SR = 10\%$. From top to bottom: the images located at the 31-th band in *chart and stuffed toy*, *feathers*, *jelly beans*, and *paints*, respectively.

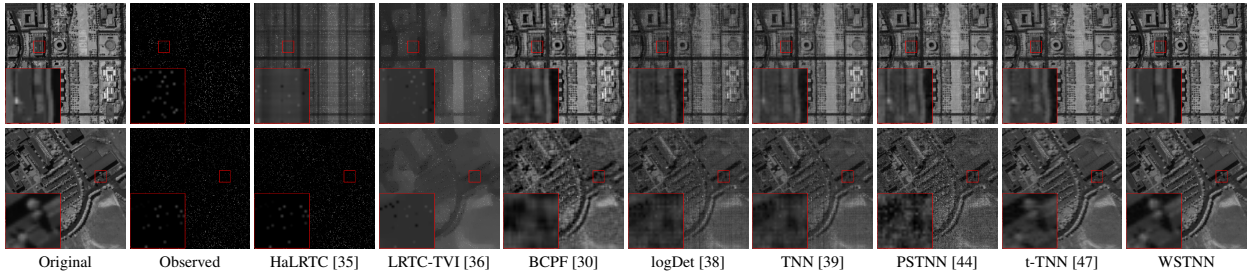


Figure 7: The completion results of the HSIs *Washington DC Mall* and *Pavia University* with $SR = 5\%$. Top row: the image located at the 70-th band in *Washington DC Mall*. Bottom row: the image located at the 85-th band in *Pavia University*.

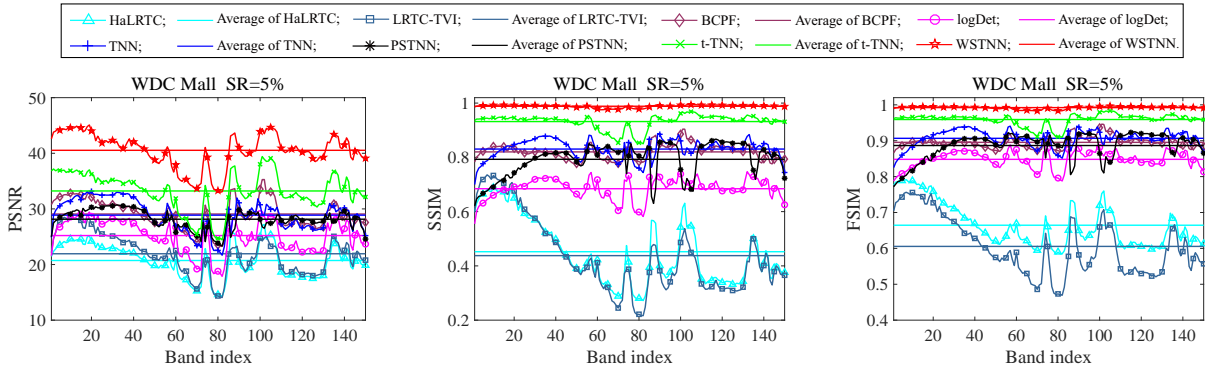


Figure 8: The PSNR, SSIM, and FSIM values of each band of the recovered HSI *Washington DC Mall* output by eight LRTC methods with $SR = 5\%$.

PSNR beyond the second best method in the test on *Washington DC Mall*. For visual comparison, in Fig. 7, we show one band in these two testing HSIs recovered by eight utilized LRTC methods with $SR = 5\%$. As observed, the proposed method is able to produce visually superior results than the compared methods. Fig. 8 shows the PSNR, SSIM and FSIM values of each band of the recovered HSI *Washington DC Mall* obtained by eight compared LRTC methods with $SR = 5\%$. From this figure, it is easy to observe that the

Table 4: The PSNR, SSIM, and FSIM values output by eight utilized LRTC methods for HSIs.

HSI	SR	5%			10%			20%			Time(s)
	Method	PSNR	SSIM	FSIM	PSNR	SSIM	FSIM	PSNR	SSIM	FSIM	
<i>Washington DC Mall</i> $256 \times 256 \times 150$	HaLRTC	20.72	0.452	0.665	24.74	0.656	0.798	29.38	0.848	0.909	76.487
	LRTC-TV1	21.93	0.437	0.605	25.89	0.638	0.759	29.11	0.824	0.893	2348.2
	BCPF	29.07	0.820	0.895	31.89	0.895	0.934	32.77	0.911	0.943	2955.9
	logDet	25.22	0.685	0.848	32.50	0.911	0.947	37.99	0.969	0.981	237.18
	TNN	28.87	0.831	0.907	32.41	0.913	0.949	36.85	0.963	0.977	294.46
	PSTNN	28.15	0.793	0.886	32.63	0.911	0.946	37.39	0.965	0.978	306.16
	t-TNN	33.23	0.932	0.959	43.96	0.994	0.996	56.99	0.997	0.998	184.23
	WSTNN	40.54	0.988	0.992	50.31	0.999	0.999	58.89	0.999	0.999	544.26
<i>Pavia University</i> $256 \times 256 \times 87$	HaLRTC	15.01	0.043	0.517	24.02	0.611	0.736	27.59	0.788	0.861	49.745
	LRTC-TV1	23.26	0.554	0.652	25.80	0.713	0.785	29.19	0.866	0.903	1427.3
	BCPF	27.64	0.726	0.835	30.39	0.836	0.898	32.07	0.884	0.928	1603.6
	logDet	26.90	0.684	0.835	32.69	0.876	0.932	39.34	0.959	0.977	140.96
	TNN	28.12	0.750	0.865	32.15	0.874	0.931	37.49	0.950	0.972	168.44
	PSTNN	23.18	0.449	0.737	32.97	0.872	0.932	38.84	0.955	0.974	181.04
	t-TNN	33.38	0.928	0.957	41.15	0.988	0.993	50.83	0.997	0.998	101.49
	WSTNN	37.26	0.976	0.983	44.48	0.995	0.997	53.92	0.999	0.999	258.78

Table 5: The PSNR, SSIM, and FSIM values output by eight utilized LRTC methods for MRI.

SR	5%			10%			20%			Time(s)
Method	PSNR	SSIM	FSIM	PSNR	SSIM	FSIM	PSNR	SSIM	FSIM	
HaLRTC	15.40	0.241	0.608	19.03	0.390	0.699	24.30	0.653	0.826	69.981
LRTC-TV1	19.36	0.597	0.702	22.84	0.748	0.805	28.19	0.891	0.908	1473.8
BCPF	22.37	0.426	0.734	23.81	0.495	0.758	24.96	0.552	0.779	1525.6
logDet	18.32	0.283	0.654	25.36	0.596	0.791	31.22	0.823	0.892	165.90
TNN	22.71	0.472	0.743	26.06	0.642	0.811	29.99	0.799	0.881	165.85
PSTNN	20.39	0.288	0.629	26.45	0.621	0.802	30.71	0.805	0.885	209.19
t-TNN	22.78	0.460	0.736	26.42	0.649	0.816	30.58	0.816	0.890	170.04
WSTNN	25.60	0.714	0.827	29.02	0.835	0.887	33.46	0.931	0.941	405.01

proposed method achieves the best performance in all bands among eight LRTC methods.

MRI completion. We test MRI⁶ data set of size $181 \times 217 \times 181$. Table 5 lists the values of PSNR, SSIM, and FSIM of the testing MRI recovered by different LRTC methods. As observed, the proposed method significantly outperforms the compared methods in terms of all evaluation indices. In Fig. 9, we show three slices obtained by different directions. It can be observed that no matter which direction they are in, the proposed method is evidently superior to the compared ones, both in recovery of abundant shape structure and texture information.

CV completion. We test CVs *news*⁷ and *hall*⁷ of size $144 \times 176 \times 3 \times 50$. For each frames, the missing elements of each channel have the same location. Table 6 lists the values of PSNR, SSIM, and FSIM of the testing CVs recovered by different LRTC methods. As observed, the proposed method has an overall better performance than the compared ones with respect to all evaluation indices. In Fig. 10, we show one frame in these two testing CVs recovered by eight compared methods with SR = 10%. We observe that the results obtained by the proposed method is superior to those obtained by the compared ones.

⁶http://brainweb.bic.mni.mcgill.ca/brainweb/selection_normal.html.

⁷<http://trace.eas.asu.edu/yuv/>.

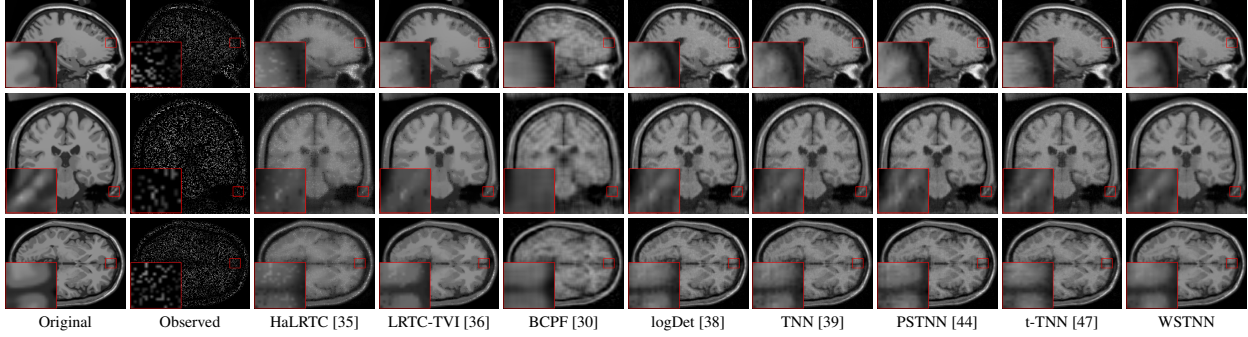


Figure 9: The completion results of the MRI data with $SR = 20\%$. From top to bottom: the images located at the 70-th horizontal slice, the 100-th lateral slice, and the 70-th frontal slice, respectively.

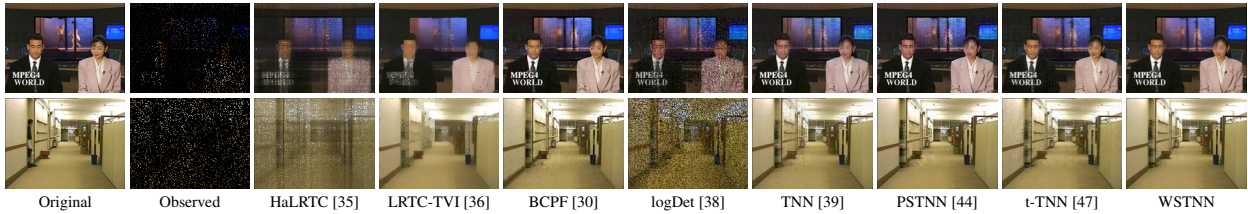


Figure 10: The completion results of the CVs *news* and *hall* with $SR = 10\%$. Top row: the image located at the 49-th frame in *news*. Bottom row: the image located at the 20-th frame in *hall*.

Table 6: The PSNR, SSIM, and FSIM values output by eight utilized LRTC methods for CVs.

CV	SR	5%			10%			20%			Time(s)
	Method	PSNR	SSIM	FSIM	PSNR	SSIM	FSIM	PSNR	SSIM	FSIM	
<i>news</i>	HaLRTC	12.59	0.413	0.649	17.67	0.596	0.767	23.92	0.816	0.886	42.53
	LRTC-TVI	18.31	0.640	0.731	20.16	0.728	0.802	23.51	0.858	0.901	768.8
	BCPF	25.49	0.779	0.881	28.05	0.857	0.919	29.87	0.897	0.939	961.3
	logDet	13.69	0.288	0.836	18.03	0.534	0.782	33.11	0.944	0.969	92.16
	TNN	21.23	0.659	0.832	29.12	0.893	0.940	32.75	0.943	0.968	97.32
	PSTNN	23.03	0.624	0.884	29.69	0.893	0.942	33.37	0.947	0.970	98.38
	t-TNN	20.65	0.605	0.804	26.92	0.844	0.919	31.91	0.934	0.965	91.36
	WSTNN	26.92	0.892	0.929	30.67	0.947	0.964	34.61	0.976	0.983	324.2
<i>hall</i>	HaLRTC	9.179	0.180	0.532	14.21	0.348	0.640	23.82	0.784	0.858	40.68
	LRTC-TVI	19.02	0.606	0.679	21.83	0.755	0.797	25.93	0.875	0.905	712.6
	BCPF	25.69	0.783	0.868	28.32	0.847	0.905	30.72	0.884	0.931	906.5
	logDet	8.192	0.073	0.503	10.80	0.162	0.553	17.30	0.498	0.750	93.94
	TNN	15.29	0.375	0.692	26.95	0.840	0.909	31.92	0.916	0.957	92.46
	PSTNN	25.31	0.765	0.874	29.39	0.876	0.935	32.42	0.920	0.959	92.27
	t-TNN	17.87	0.442	0.718	27.86	0.844	0.917	32.39	0.918	0.957	84.98
	WSTNN	26.99	0.875	0.920	31.13	0.925	0.956	34.36	0.953	0.973	347.6

HSV completion. We test HSV⁸ of size $120 \times 120 \times 33 \times 31$. Specifically, this HSV has 31 frames and each frame has 33 bands from 400nm to 720nm wavelength with a 10nm step [58]. Table 7 lists the values of PSNR, SSIM, and FSIM of the testing HSV recovered by different LRTC methods. As observed, the proposed method consistently achieves the highest values in terms of all evaluation indexes, e.g., no matter what the SR is set as, the proposed method achieves around 4 dB gain in PSNR beyond the second

⁸<http://openremotesensing.net/knowledgebase/hyperspectral-video/>.

Table 7: The PSNR, SSIM, and FSIM values output by eight utilized LRTC methods for HSV.

SR	5%			10%			20%			Time(s)
Method	PSNR	SSIM	FSIM	PSNR	SSIM	FSIM	PSNR	SSIM	FSIM	
HaLRTC	9.008	0.115	0.519	10.46	0.194	0.565	13.41	0.338	0.652	162.77
LRTC-TVI	22.09	0.686	0.791	27.08	0.835	0.891	32.19	0.931	0.959	5121.5
BCPF	27.75	0.855	0.907	30.23	0.902	0.934	31.69	0.917	0.945	5840.6
logDet	31.01	0.912	0.948	38.94	0.975	0.984	44.52	0.991	0.995	446.61
TNN	33.68	0.946	0.968	38.02	0.974	0.984	42.94	0.989	0.993	487.95
PSTNN	32.93	0.934	0.960	38.53	0.975	0.985	43.41	0.989	0.994	423.32
t-TNN	29.43	0.894	0.931	34.37	0.957	0.971	40.11	0.986	0.990	391.87
WSTNN	37.61	0.979	0.986	43.67	0.994	0.996	49.11	0.997	0.998	1228.3

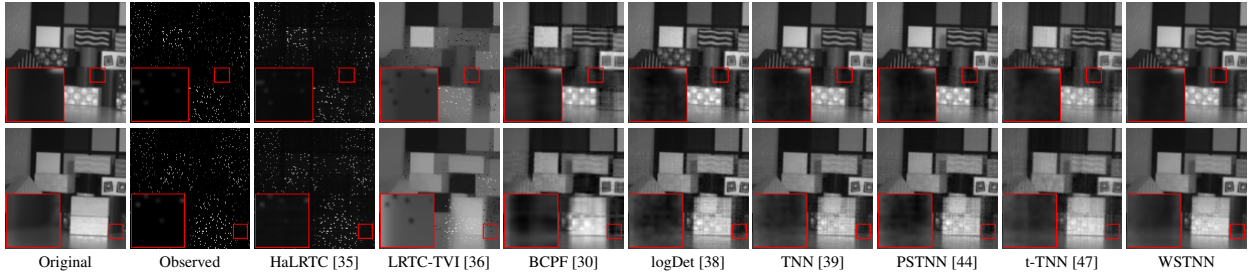


Figure 11: The completion results of the HSV with $SR = 5\%$. Top row: the image located at the 15-th band and the 7-th frame. Bottom row: the image located at the 25-th band and the 30-th frame.

best method. In Fig. 11, we show two images located at different frames and different bands in the HSV recovered by eight compared methods with $SR = 5\%$. We observe that the proposed method is evidently superior to the compared ones, especially in recovery of texture information.

5.2. Tensor robust principal component analysis

In this section, we evaluate the performance of the proposed WSTNN-based TRPCA method by synthetic data and HSI denoising. The compared TRPCA methods include SNN [40] and TNN [46].

Parameter selection. In all tests, the stopping criterion lies on the RelCha of two successive recovered tensors, i.e., $\text{RelCha} = \frac{\|\mathcal{L}^{(p+1)} - \mathcal{L}^{(p)}\|_F}{\|\mathcal{L}^{(p)}\|_F} < 10^{-4}$. The tuning parameter λ is set to be

$$\lambda = \sum_{1 \leq k_1 < k_2 \leq N} \frac{\alpha_{k_1 k_2}}{\sqrt{\max(n_{k_1}, n_{k_2}) d_{k_1 k_2}}} \text{ with } d_{k_1 k_2} = \prod_{s \neq k_1, k_2} n_s.$$

Letting the threshold parameter $\tau = \alpha/\beta$, then the penalty parameter ρ is set to be $\rho = 1/\text{mean}(\tau)$. This means that only the weight α and the threshold τ need to be adjusted. Table 8 shows these two parameters setting in the proposed WSTNN-based TRPCA method on different data, where α is chosen by the strategy of the weight selection in Section 3, τ is set to be $\omega \times \text{ones}(N(N-1)/2, 1)$, and ω is empirically selected from a candidate set: $\{1, 10, 50, 100, 500, 1000, 10000\}$.

Synthetic data denoising. We test three-way tensors of size $30 \times 30 \times 30$ and four-way tensors of size $30 \times 30 \times 30 \times 30$ with different N -tubal rank and random salt-pepper noise level (NL). The N -tubal rank are set to be $r \times \text{ones}(N(N-1)/2, 1)$ ($r = 1, 2, \dots, 20$) and the NLs are set to be $0.025 \times l$ ($l = 1, 2, \dots, 20$). For each pair of N -tubal rank and NL, we conduct 50 independent tests and calculate the success rate. Fig. 12 shows the success rates for varying N -tubal rank and varying NLs. The results illustrate that the proposed WSTNN-based TRPCA method is more robust and preferable than the TNN-based method [46].

Table 8: Parameters setting in the proposed WSTNN-based TRPCA method on different data.

Test	Tensor	α	τ
synthetic data denoising	three-way tensor	(1,1,1)/3	(10,10,10)
	four-way tensor	(1,1,1,1,1)/6	(50,50,50,50,50)
HSI denoising	three-way tensor	(0.001,1,1)/2.001	(100,100,100)

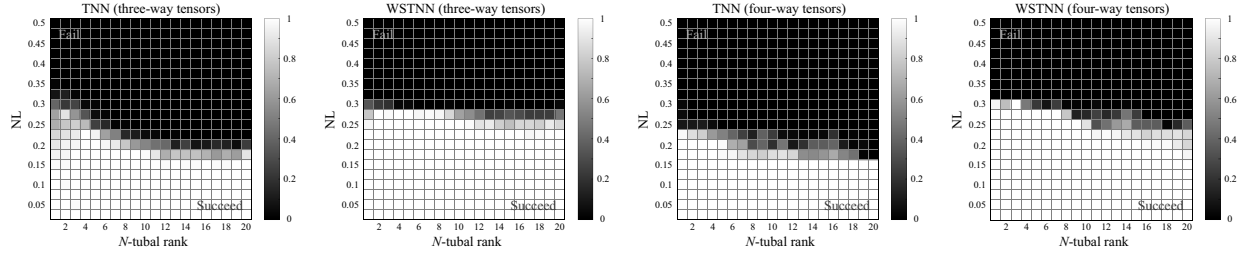


Figure 12: The success rates for synthetic data with varying N -tubal rank and varying NLs. The left two are the results of TNN-based TRPCA method [46] and the proposed WSTNN-based TRPCA method on three-way tensors. The right two are the results of TNN-based TRPCA method [46] and the proposed WSTNN-based TRPCA method on four-way tensors. The gray magnitude represents the success rates.

Table 9: The PSNR, SSIM, and FSIM values output by three utilized TRPCA methods for HSIs.

HSI	NL	0.2			0.4			Time(s)
	Method	PSNR	SSIM	FSIM	PSNR	SSIM	FSIM	
<i>Washington</i>	SNN	31.48	0.927	0.950	28.19	0.848	0.902	79.822
<i>DC Mall</i> $256 \times 256 \times 150$	TNN	43.87	0.992	0.994	35.82	0.953	0.973	172.81
	WSTNN	50.49	0.999	0.999	42.29	0.993	0.995	385.39
<i>Pavia</i>	SNN	28.14	0.877	0.899	26.16	0.787	0.834	56.238
<i>University</i> $256 \times 256 \times 87$	TNN	38.97	0.983	0.988	35.42	0.958	0.975	120.28
	WSTNN	39.21	0.995	0.997	36.48	0.988	0.993	243.89

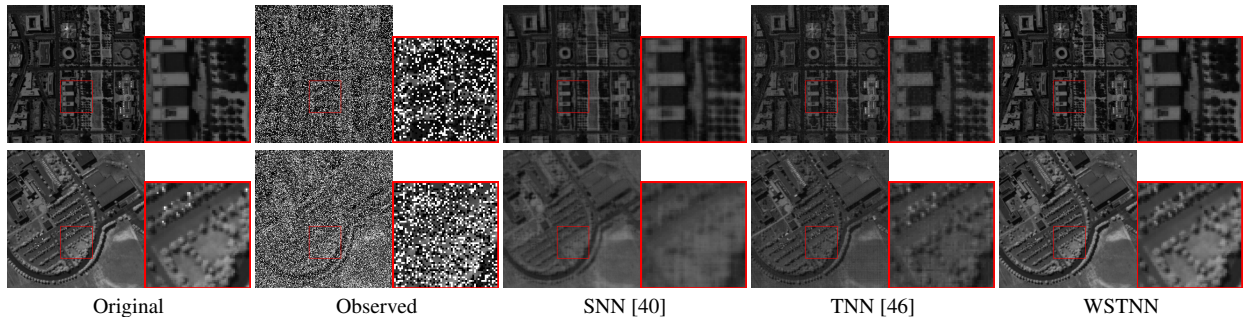


Figure 13: The denoising results of the HSI *Washington DC Mall* and *Pavia University* with $NL = 0.4$. Top row: the image located at the 150-th band in *Washington DC Mall*. Bottom row: the image located at the 87-th band in *Pavia University*.

HSI denoising. We test HSIs *Washington DC Mall* and the *Pavia University* data sets. The NL of random salt-pepper noise are set to be 0.2 and 0.4. Table 9 lists PSNR, SSIM, and FSIM values of the testing HSIs recovered by different methods. From these results, we observe that our method evidently performs better than other competing ones in terms of all the evaluation measures. In Fig. 13, we show one band in these two HSIs. As observed, our WSTNN-based TRPCA method achieves the best visual results among three compared methods, both in the noise removing and the details preserving.

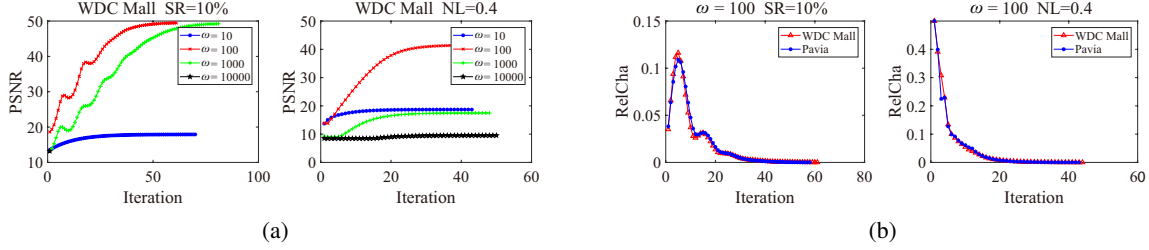


Figure 14: (a) The PSNR values with respect to the iteration for different values of parameter τ . Left column: completion tests. Right column: denoising tests. (b) The RelCha values with respect to the iteration with parameter $\tau = (100, 100, 100)$. Left column: completion tests. Right column: denoising tests.

5.3. Parameter and convergence analysis

In this section, we test the effects of the threshold parameter τ and the convergence of the proposed ADMM in the proposed LRTC and TRPCA problems. All tests are based on the HSI *Washington DC Mall*.

Effects of threshold parameter. We set SR to 10% in completion tests and NL to 0.4 in denoising tests. And τ is set to be $\tau = (\omega, \omega, \omega)$. The results is presented in Fig. 14(a). As observed, for parameter τ , too large or too small values output failure results, while the moderate values obtain the best results. This observation is consistent with the theoretical analysis. That is, for completion tests, if the parameter τ is too large (e.g., (10000, 10000, 10000)), all the singular values are replaced by 0, the algorithm iterates only one step and outputs the partial observation tensor \mathcal{F} . If the parameter τ is too small (e.g., (10, 10, 10)), the singular values after performing the t-SVT (in Theorem 3) contain many corrupted information, i.e., it is not consistent with the low-rank prior of the underlying tensor. Similarly, for denoising tests, if the parameter τ is too large or too small, the low-rank term is out of action. Under the guidance of Fig. 14(a), parameter τ is set to be (100, 100, 100) in all experiments conducted on real-world data.

Convergence analysis. Owing to the use of ADMM framework and the convexity of the objective functions, the convergence of two developed algorithms is guaranteed theoretically. Empirically, such the convergence can be visually observed from Fig. 14(b), where τ is set to be (100, 100, 100).

6. Conclusions

In this paper, we defined the mode- $k_1 k_2$ tensor unfolding to reorder the elements of an N -way tensor into a three-way tensor, and then performed the t-SVD on each mode- $k_1 k_2$ unfolding tensor to depict the correlations along different modes. Based on this, we proposed the corresponding tensor N -tubal rank and its convex relaxation WSTNN. To illustrate the effectiveness of the proposed N -tubal rank and WSTNN, we applied WSTNN to two typical LRTR problems, LRTC and TRPCA problems, and proposed the WSTNN-based LRTC and TRPCA models. Meanwhile, two efficient ADMM-based algorithms were developed to solve the proposed models. Numerical results demonstrated the proposed method effectively exploit the correlations along all modes while preserving the intrinsic structure of the underlying tensor.

Acknowledgments

This work is supported by the National Natural Science Foundation of China (61772003, 61876203), the Fundamental Research Funds for the Central Universities (ZYGX2016J132, 31020180QD126), the National Postdoctoral Program for Innovative Talents (BX20180252), and the Project funded by China Postdoctoral Science Foundation (2018M643611).

References

- [1] T. G. Kolda and B. W. Bader, “Tensor decompositions and applications,” *SIAM Review*, vol. 51, no. 3, pp. 455–500, 2009.
- [2] T.-H. Ma, T.-Z. Huang, and X.-L. Zhao, “Group-based image decomposition using 3-D cartoon and texture priors,” *Information Sciences*, vol. 328, pp. 510–527, 2016.
- [3] Y.-M. Huang, H.-Y. Yan, Y.-W. Wen, and X. Yang, “Rank minimization with applications to image noise removal,” *Information Sciences*, vol. 429, pp. 147–163, 2018.
- [4] T.-X. Jiang, T.-Z. Huang, X.-L. Zhao, L.-J. Deng, and Y. Wang, “Fastderain: A novel video rain streak removal method using directional gradient priors,” *IEEE Transactions on Image Processing*, doi: 10.1109/TIP.2018.2880512, 2018.
- [5] T. Xie, S. Li, L. Fang, and L. Liu, “Tensor completion via nonlocal low-rank regularization,” *IEEE Transactions on Cybernetics*, doi:10.1109/TCYB.2018.2825598, 2018.
- [6] B. Madathil and S. N. George, “Twist tensor total variation regularized-reweighted nuclear norm based tensor completion for video missing area recovery,” *Information Sciences*, vol. 423, pp. 376–397, 2018.
- [7] Y. Wang, D. Meng, and M. Yuan, “Sparse recovery: from vectors to tensors,” *National Science Review*, vol. 5, no. 5, pp. 756–767, 2018.
- [8] X. Zhang, “A nonconvex relaxation approach to low-rank tensor completion,” *IEEE Transactions on Neural Networks and Learning Systems*, doi:10.1109/TNNLS.2018.2872583, 2018.
- [9] Y. Wang, J. Peng, Q. Zhao, Y. Leung, X.-L. Zhao, and D. Meng, “Hyperspectral image restoration via total variation regularized low-rank tensor decomposition,” *IEEE Journal of Selected Topics in Applied Earth Observations and Remote Sensing*, vol. 11, no. 99, pp. 1–19, 2017.
- [10] X.-L. Zhao, F. Wang, and M. K. Ng, “A new convex optimization model for multiplicative noise and blur removal,” *SIAM Journal on Imaging Sciences*, vol. 7, no. 1, pp. 456–475, 2014.
- [11] X. Fu, W. K. Ma, J. M. Bioucas-Dias, and T. H. Chan, “Semiblind hyperspectral unmixing in the presence of spectral library mismatches,” *IEEE Transactions on Geoscience and Remote Sensing*, vol. 54, no. 9, pp. 5171–5184, 2016.
- [12] Y. Chang, L. Yan, H. Fang, S. Zhong, and Z. Zhang, “Weighted low-rank tensor recovery for hyperspectral image restoration,” *arXiv preprint arXiv:1709.00192*, 2017.
- [13] S. Li, R. Dian, L. Fang, and J. M. Bioucas-Dias, “Fusing hyperspectral and multispectral images via coupled sparse tensor factorization,” *IEEE Transactions on Image Processing*, vol. 27, no. 8, pp. 4118–4130, 2018.
- [14] T.-Y. Ji, N. Yokoya, X.-X. Zhu, and T.-Z. Huang, “Nonlocal tensor completion for multitemporal remotely sensed images’ inpainting,” *IEEE Transactions on Geoscience and Remote Sensing*, vol. 56, no. 6, pp. 3047–3061, 2018.
- [15] L. Zhuang and J. M. Bioucas-Dias, “Fast hyperspectral image denoising and inpainting based on low-rank and sparse representations,” *IEEE Journal of Selected Topics in Applied Earth Observations and Remote Sensing*, vol. 11, no. 3, pp. 730–742, 2018.
- [16] I. Kajo, N. Kamel, Y. Ruichek, and A. S. Malik, “SVD-based tensor-completion technique for background initialization,” *IEEE Transactions on Image Processing*, vol. 27, no. 6, pp. 3114–3126, 2018.
- [17] W. Cao, Y. Wang, J. Sun, D. Meng, C. Yang, A. Cichocki, and Z. Xu, “Total variation regularized tensor RPCA for background subtraction from compressive measurements,” *IEEE Transactions on Image Processing*, vol. 25, no. 9, pp. 4075–4090, 2016.

- [18] T.-X. Jiang, T.-Z. Huang, X.-L. Zhao, L.-J. Deng, and Y. Wang, “A novel tensor-based video rain streaks removal approach via utilizing discriminatively intrinsic priors,” in *the IEEE Conference on Computer Vision and Pattern Recognition (CVPR)*, 2017, pp. 4057–4066.
- [19] W. Wei, L. Yi, Q. Xie, Q. Zhao, D. Meng, and Z. Xu, “Should we encode rain streaks in video as deterministic or stochastic?” in *the IEEE Conference on Computer Vision and Pattern Recognition (CVPR)*, 2017, pp. 2516–2525.
- [20] M. Li, Q. Xie, Q. Zhao, W. Wei, S. Gu, J. Tao, and D. Meng, “Video rain streak removal by multiscale convolutional sparse coding,” in *the IEEE Conference on Computer Vision and Pattern Recognition (CVPR)*, 2018, pp. 6644–6653.
- [21] T.-Y. Ji, T.-Z. Huang, X.-L. Zhao, T.-H. Ma, and G. Liu, “Tensor completion using total variation and low-rank matrix factorization,” *Information Sciences*, vol. 326, pp. 243–257, 2016.
- [22] T.-X. Jiang, T.-Z. Huang, X.-L. Zhao, T.-Y. Ji, and L.-J. Deng, “Matrix factorization for low-rank tensor completion using framelet prior,” *Information Sciences*, vol. 436, pp. 403–417, 2018.
- [23] E. J. Candès and B. Recht, “Exact matrix completion via convex optimization,” *Foundations of Computational Mathematics*, vol. 9, no. 6, pp. 717–772, 2009.
- [24] J.-F. Cai, E. J. Candès, and Z. Shen, “A singular value thresholding algorithm for matrix completion,” *SIAM Journal on Optimization*, vol. 20, no. 4, pp. 1956–1982, 2010.
- [25] Y. Peng, J. Suo, Q. Dai, and W. Xu, “Reweighted low-rank matrix recovery and its application in image restoration,” *IEEE Transactions on Cybernetics*, vol. 44, no. 12, pp. 2418–2430, 2014.
- [26] M. A. Davenport and J. Romberg, “An overview of low-rank matrix recovery from incomplete observations,” *IEEE Journal of Selected Topics in Signal Processing*, vol. 10, no. 4, pp. 608–622, 2016.
- [27] C. J. Hillar and L.-H. Lim, “Most tensor problems are NP-hard,” *Journal of the ACM*, vol. 60, no. 6, pp. 45:1–45:39, 2013.
- [28] J. D. Carroll, S. Pruzansky, and J. B. Kruskal, “Candelinc: A general approach to multidimensional analysis of many-way arrays with linear constraints on parameters,” *Psychometrika*, vol. 45, no. 1, pp. 3–24, 1980.
- [29] M. Zhou, Y. Liu, Z. Long, L. Chen, and C. Zhu, “Tensor rank learning in CP decomposition via convolutional neural network,” *Signal Processing: Image Communication*, doi:10.1016/j.image.2018.03.017, 2018.
- [30] Q. Zhao, L. Zhang, and A. Cichocki, “Bayesian CP factorization of incomplete tensors with automatic rank determination,” *IEEE Transactions on Pattern Analysis and Machine Intelligence*, vol. 37, no. 9, pp. 1751–1763, 2015.
- [31] L. R. Tucker, “Some mathematical notes on three-mode factor analysis,” *Psychometrika*, vol. 31, no. 3, pp. 279–311, 1966.
- [32] S. Gandy, B. Recht, and I. Yamada, “Tensor completion and low-n-rank tensor recovery via convex optimization,” *Inverse Problems*, vol. 27, no. 2, p. 025010, 2011.
- [33] D. Kressner, M. Steinlechner, and B. Vandereycken, “Low-rank tensor completion by riemannian optimization,” *BIT Numerical Mathematics*, vol. 54, no. 2, pp. 447–468, 2014.
- [34] X. Li, M. K. Ng, G. Cong, Y. Ye, and Q. Wu, “MR-NTD: Manifold regularization nonnegative tucker decomposition for tensor data dimension reduction and representation,” *IEEE Transactions on Neural Networks and Learning Systems*, vol. 28, no. 8, pp. 1787–1800, 2017.
- [35] J. Liu, P. Musialski, P. Wonka, and J. Ye, “Tensor completion for estimating missing values in visual data,” *IEEE Transactions on Pattern Analysis and Machine Intelligence*, vol. 35, no. 1, pp. 208–220, 2013.

- [36] X. Li, Y. Ye, and X. Xu, “Low-rank tensor completion with total variation for visual data inpainting,” in *AAAI*, 2017, pp. 2210–2216.
- [37] M. E. Kilmer, K. Braman, N. Hao, and R. C. Hoover, “Third-order tensors as operators on matrices: A theoretical and computational framework with applications in imaging,” *SIAM Journal on Matrix Analysis and Applications*, vol. 34, no. 1, pp. 148–172, 2013.
- [38] T.-Y. Ji, T.-Z. Huang, X.-L. Zhao, T.-H. Ma, and L.-J. Deng, “A non-convex tensor rank approximation for tensor completion,” *Applied Mathematical Modelling*, vol. 48, pp. 410–422, 2017.
- [39] Z. Zhang and S. Aeron, “Exact tensor completion using t-SVD,” *IEEE Transactions on Signal Processing*, vol. 65, no. 6, pp. 1511–1526, 2017.
- [40] D. Goldfarb and Z. T. Qin, “Robust low-rank tensor recovery: Models and algorithms,” *SIAM Journal on Matrix Analysis and Applications*, vol. 35, no. 1, pp. 225–253, 2014.
- [41] M. K. Ng, Q. Yuan, L. Yan, and J. Sun, “An adaptive weighted tensor completion method for the recovery of remote sensing images with missing data,” *IEEE Transactions on Geoscience and Remote Sensing*, vol. 55, no. 6, pp. 3367–3381, 2017.
- [42] Q. Xie, Q. Zhao, D. Meng, and Z. Xu, “Kronecker-basis-representation based tensor sparsity and its applications to tensor recovery,” *IEEE Transactions on Pattern Analysis and Machine Intelligence*, vol. 40, no. 8, pp. 1888–1902, 2018.
- [43] Z. Zhang, G. Ely, S. Aeron, N. Hao, and M. Kilmer, “Novel methods for multilinear data completion and denoising based on tensor-SVD,” in *the IEEE Conference on Computer Vision and Pattern Recognition (CVPR)*, 2014, pp. 3842–3849.
- [44] T.-X. Jiang, T.-Z. Huang, X.-L. Zhao, and L.-J. Deng, “A novel nonconvex approach to recover the low-tubal-rank tensor data: when t-SVD meets PSSV,” *arXiv preprint arXiv:1712.05870*, 2017.
- [45] P. Zhou and J. Feng, “Outlier-robust tensor PCA,” in *the IEEE Conference on Computer Vision and Pattern Recognition (CVPR)*, 2017, pp. 3938–3946.
- [46] C. Lu, J. Feng, Y. Chen, W. Liu, Z. Lin, and S. Yan, “Tensor robust principal component analysis: Exact recovery of corrupted low-rank tensors via convex optimization,” in *the IEEE Conference on Computer Vision and Pattern Recognition (CVPR)*, 2016, pp. 5249–5257.
- [47] W. Hu, D. Tao, W. Zhang, Y. Xie, and Y. Yang, “The twist tensor nuclear norm for video completion,” *IEEE Transactions on Neural Networks and Learning Systems*, vol. 28, no. 12, pp. 2961–2973, 2017.
- [48] P. Zhou, C. Lu, Z. Lin, and C. Zhang, “Tensor factorization for low-rank tensor completion,” *IEEE Transactions on Image Processing*, vol. 27, no. 3, pp. 1152–1163, 2018.
- [49] C. Lu, J. Feng, Y. Chen, W. Liu, Z. Lin, and S. Yan, “Tensor robust principal component analysis with a new tensor nuclear norm,” *arXiv preprint arXiv:1804.03728*, 2018.
- [50] Y. Xie, D. Tao, W. Zhang, Y. Liu, L. Zhang, and Y. Qu, “On unifying multi-view self-representations for clustering by tensor multi-rank minimization,” *International Journal of Computer Vision*, pp. 1–23, 2016.
- [51] A. Bibi and B. Ghanem, “High order tensor formulation for convolutional sparse coding,” in *the IEEE Conference on Computer Vision and Pattern Recognition (CVPR)*, 2017, pp. 1772–1780.
- [52] S. Xue, W. Qiu, F. Liu, and X. Jin, “Low-rank tensor completion by truncated nuclear norm regularization,” *arXiv preprint arXiv:1712.00704*, 2017.
- [53] O. Semerci, N. Hao, M. E. Kilmer, and E. L. Miller, “Tensor-based formulation and nuclear norm regularization for multienergy computed tomography,” *IEEE Transactions on Image Processing*, vol. 23, no. 4, pp. 1678–1693, 2014.

- [54] X.-L. Zhao, F. Wang, T.-Z. Huang, M. K. Ng, and R. J. Plemmons, “Deblurring and sparse unmixing for hyperspectral images,” *IEEE Transactions on Geoscience and Remote Sensing*, vol. 51, no. 7, pp. 4045–4058, 2013.
- [55] T.-H. Ma, Y. Lou, and T.-Z. Huang, “Truncated ℓ_{1-2} models for sparse recovery and rank minimization,” *SIAM Journal on Imaging Sciences*, vol. 10, no. 3, pp. 1346–1380, 2017.
- [56] Z. Wang, A. C. Bovik, H. R. Sheikh, and E. P. Simoncelli, “Image quality assessment: from error visibility to structural similarity,” *IEEE Transactions on Image Processing*, vol. 13, no. 4, pp. 600–612, 2004.
- [57] L. Zhang, L. Zhang, X. Mou, and D. Zhang, “FSIM: A feature similarity index for image quality assessment,” *IEEE Transactions on Image Processing*, vol. 20, no. 8, pp. 2378–2386, 2011.
- [58] A. Mian and R. Hartley, “Hyperspectral video restoration using optical flow and sparse coding,” *Optics Express*, vol. 20, no. 10, pp. 10 658–10 673, 2012.